






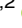




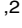











# Selective synthesis of higher manganese silicides: a new $Mn_{17}Si_{30}$ phase, its electronic, transport, and optical properties in comparison with $Mn_4Si_7$

Ivan A. Tarasov<sup>1,\*</sup> , Maxim A. Visotin<sup>1,2</sup> , Tatiana V. Kuznetzova<sup>3,4</sup> , Aleksandr S. Aleksandrovsky<sup>1,5</sup> , Leonid A. Solovyov<sup>6</sup> , Aleksandr A. Kuzubov<sup>2</sup> , Kristina M. Nikolaeva<sup>2</sup> , Aleksandr S. Fedorov<sup>1,2</sup> , Anton S. Tarasov<sup>1,2</sup> , Felix N. Tomilin<sup>1,2</sup> , Michail N. Volochaev<sup>1,7</sup> , Ivan A. Yakovlev<sup>1</sup> , Tatiana E. Smolyarova<sup>1,2</sup> , Aleksandr A. Ivanenko<sup>1</sup> , Victoria I. Pryahina<sup>8</sup> , Alexander A. Esin<sup>8</sup> , Yuri M. Yarmoshenko<sup>3</sup> , Vladimir Ya Shur<sup>8</sup> , Sergey N. Varnakov<sup>1</sup> , and Sergey G. Ovchinnikov<sup>1,2</sup> 

<sup>1</sup> Federal Research Center KSC SB RAS, Kirensky Institute of Physics, Krasnoyarsk, Russia 660036

<sup>2</sup> Siberian Federal University, Krasnoyarsk, Russia 660041

<sup>3</sup> M.N. Miheev Institute of Metal Physics of the UB RAS, Yekaterinburg, Russia 620108

<sup>4</sup> Institute of Physics and Technology, Ural Federal University, Yekaterinburg, Russia 620002

<sup>5</sup> Siberian Federal University, Institute of Nanotechnology, Quantum Chemistry and Spectroscopy, Krasnoyarsk, Russia 660041

<sup>6</sup> Institute of Chemistry and Chemical Technology, Federal Research Center KSC SB RAS, Krasnoyarsk, Russia 660036

<sup>7</sup> Siberian State Aerospace University, Krasnoyarsk, Russia 660014

<sup>8</sup> Institute of Natural Sciences, Ural Federal University, Yekaterinburg, Russia 620000

Received: 4 December 2017

Accepted: 1 February 2018

Published online:

20 February 2018

© Springer Science+Business Media, LLC, part of Springer Nature 2018

## ABSTRACT

The electronic structure, transport and optical properties of thin films of  $Mn_4Si_7$  and  $Mn_{17}Si_{30}$  higher manganese silicides (HMS) with the Nowotny “chimney-ladder” crystal structure are investigated using different experimental techniques and density functional theory calculations. Formation of new  $Mn_{17}Si_{30}$  compound through selective solid-state reaction synthesis proposed and its crystal structure is reported for the first time, the latter belonging to  $I-42d$ . Absorption measurements show that both materials demonstrate direct interband transitions around 0.9 eV, while the lowest indirect transitions are observed close to 0.4 eV. According to ab initio calculations, ideally structured  $Mn_{17}Si_{30}$  is a degenerate n-type semiconductor; however, the Hall measurements on the both investigated materials reveal their p-type conductivity and degenerate nature. Such a shift of the Fermi level is attributed to introduction of silicon vacancies in accordance with our DFT calculations and optical characteristics in low photon energy range (0.076–0.4 eV). The Hall mobility for  $Mn_{17}Si_{30}$  thin film was found to be  $25 \text{ cm}^2/\text{V s}$  at  $T = 77 \text{ K}$ , being the highest among all HMS known before. X-ray photoelectron spectroscopy discloses a presence of plasmon satellites in the  $Mn_4Si_7$  and  $Mn_{17}Si_{30}$  valence band spectra.

Address correspondence to E-mail: tia@iph.krasn.ru

<https://doi.org/10.1007/s10853-018-2105-y>

Experimental permittivity spectra for the  $\text{Mn}_4\text{Si}_7$  and  $\text{Mn}_{17}\text{Si}_{30}$  compounds in a wide range (0.076–6.54 eV) also indicate degenerate nature of both materials and put more emphasis upon the intrinsic relationship between lattice defects and optical properties.

## Introduction

Higher manganese silicides (HMS) are attractive materials for thermoelectric [1–4] and photovoltaic power generation, light emission and detection [5]. The dimensionless figure-of-merit of HMS thermoelectric performance lies in the range of 0.4–0.7 at 800 K, which is suitable for their application to the recovery of enormous waste heat from automobile engines. Higher manganese thin-film-based microstructured thermoelectric modules can be applied for transformation of the waste heat from different electronic components in outer space due to their high-temperature stability. Despite a great number of works on HMS synthesis and investigation of their physical properties, both in bulk and low-dimensional nanostructured forms, several technological and scientifically important issues remain not fully explored. HMS family includes several homologous phases with Nowotny chimney-ladder (NCL) tetragonal crystal structure that is composed of tetragonal manganese  $\beta$ -Sn-like chimney subcell and double-helically arranged silicon subcell [3]. Five different commensurate HMS compounds in chemical composition range  $\text{MnSi}_{1.72-1.75}$ , which are  $\text{Mn}_{11}\text{Si}_{19}$  ( $\text{MnSi}_{1.727}$ ),  $\text{Mn}_{15}\text{Si}_{26}$  ( $\text{MnSi}_{1.733}$ ),  $\text{Mn}_{26}\text{Si}_{45}$  ( $\text{MnSi}_{1.730}$ ),  $\text{Mn}_{27}\text{Si}_{47}$  ( $\text{MnSi}_{1.741}$ ) и  $\text{Mn}_4\text{Si}_7$  ( $\text{MnSi}_{1.750}$ ) [6–9], have been reported so far with the atomic position determined by X-ray diffraction (XRD) on bulk samples. Along with these well-known HMS phases, other HMS compounds such as  $\text{Mn}_7\text{Si}_{12}$  ( $\text{MnSi}_{1.714}$ ),  $\text{Mn}_{26}\text{Si}_{45}$  ( $\text{MnSi}_{1.731}$ ),  $\text{Mn}_{19}\text{Si}_{33}$  ( $\text{MnSi}_{1.737}$ ), and  $\text{Mn}_{39}\text{Si}_{68}$  ( $\text{MnSi}_{1.744}$ ) have been described in XRD and electron diffraction studies on nanosized samples, thin films, nanowires, nanorods [10–12]. Nevertheless, the list of possible homologous HMS phases may be not fully determined because there are evidences of existence of other NCL commensurate phases in other material systems as well as incommensurate HMS phases. This variety of the homologous HMS phases, where Si content varies only in the range of 63.2–63.64 at. %, gives rise to the uncertainty in experimental

studies of the HMS transport and optical properties. The existence of a direct gap near the range of 0.7–0.96 eV and an indirect gap close to 0.4 eV, reported in different studies [5], appears to be a common property of the HMS family. In *ab initio* study, Migas et al. [13] have shown that four well-known HMS phases possess similar band dispersion near the energy gap, which makes it difficult to distinguish between them using resistivity and optical measurements. Along with these theoretical findings, the key influence of the stoichiometry and lattice defects [14], such as stacking faults and silicon vacancies [13], on electronic structure has also been revealed. Specifically, silicon vacancies and stacking faults lead to a metallisation of the electronic spectrum and a magnetic state of half-metallic nature in  $\text{Mn}_4\text{Si}_7$ ,  $\text{Mn}_{11}\text{Si}_{19}$ ,  $\text{Mn}_{15}\text{Si}_{26}$ , and  $\text{Mn}_{27}\text{Si}_{47}$  phases, while the addition of Si atom to the unoccupied positions in different HMS structure results in non-degenerate nature appearance. Dislocations, stacking faults, silicon and manganese vacancies, slight gradual shifts of silicon helices relative to each other are typical for HMS compounds [15, 16]. Along with the reasons mentioned above, MnSi phase inclusions formed during HMS phase transformation and coexistence of microscopic domains formed of different commensurate and incommensurate HMS compounds, in one sample, could explain the ambiguity existed in experimental results.

It is well known the higher manganese silicides behave like p-type degenerate semiconductors [13] and only  $\text{Mn}_4\text{Si}_7$  phase of all HMS has non-degenerate nature. Thus, the HMS phases are usually exploited as p-legs in thermoelectric modules, where pairing with other non-HMS n-type materials can diminish the durability of the TE module due to the difference between their thermal expansion coefficients. To overcome this problem, one can utilise n-type HMS-like phase. The prediction about p- to n-type conductivity transition due to the partial substitution of Mn atoms by Fe atoms was experimentally proved by different groups [17]. Some

theoretical works have been done on the substituted  $\text{Mn}_4\text{Si}_7$  compound with many different atoms [18, 19]. Moreover, there are reports of the synthesis of n-type HMS with no substitution [20–23]. However, these works do not contain exact HMS phase identification. According to the valence electron count (VEC) concept, a crossover from p-type to n-type is observed close to the VEC value of 14.02 [17].  $\text{Mn}_4\text{Si}_7$  (1.75) phase is the most silicon rich phase from HMS family. Its VEC value equals to 14 electrons atoms per one Mn atom and corresponds to the maximum among pure known HMS compounds. Flihier et al. [24] reported that partial substitution of Mn with Cr or Fe atoms causes the formation of new HMS-like phases with Si/T ratio ( $T$ —metal atoms) higher than 1.75 ( $\text{Mn}_4\text{Si}_7$ ), which are  $(\text{Mn}_{0.8}\text{Cr}_{0.2})_{29}\text{Si}_{51}$  (1.758) and  $(\text{Mn}_{0.8}\text{Cr}_{0.25})_{17}\text{Si}_{30}$  (1.765). Thus, one can expect that pure Mn–Si with such crystal structure can also exist. VEC for these compounds reaches 14.02 and 14.06, respectively, i.e.  $\text{Mn}_{29}\text{Si}_{51}$  and  $\text{Mn}_{17}\text{Si}_{30}$  should demonstrate n-type conductivity.

Here we report ab initio theoretical and experimental study of the electronic, transport and optical properties of  $\text{Mn}_{17}\text{Si}_{30}$  phase. The possibility of  $\text{Mn}_{17}\text{Si}_{30}$  thin film controllable growth by solid-state reaction method is discussed below. To carry out a comparison of the new phase physical properties with other HMS phases, the  $\text{Mn}_4\text{Si}_7$  compound is taken as a reference.

## Theoretical methods and experimental details

The electronic structure of  $\text{Mn}_{17}\text{Si}_{30}$  and type  $\text{Mn}_4\text{Si}_7$  silicides were calculated in the framework of the density functional theory (DFT) implemented in VASP 5.3 program package [25, 26] using the plane wave basis and the projector augmented wave (PAW) formalism [27]. To describe the exchange–correlation functional, we used the generalised gradient approximation (GGA) in the form proposed by Perdew, Burke, and Ernzerhof (PBE) [28]. For optimisation of the unit cell geometry, the first Brillouin zone in the reciprocal space was sampled on  $5 \times 5 \times 3$  and  $5 \times 5 \times 2$  meshes chosen according to the Monkhorst–Pack scheme, for  $\text{Mn}_4\text{Si}_7$  and  $\text{Mn}_{17}\text{Si}_{30}$ , respectively. In all calculations, the cutoff energy  $E_{\text{cutoff}}$  was equal to 400 eV. The optimisation of the geometry was performed until the maximum values

of the forces acting on atoms were less than 0.05 eV/Å. The frequency-dependent dielectric tensors were calculated within the linear response theory [29].

To obtain HMS thin films, the solid-state reaction method was used. Formation of the HMS phases occurs due to thermal diffusion of silicon atoms from the substrate, and also from amorphous layers of silicon and manganese mixture with a constant and variable Si/Mn ratio. The approach proposed for synthesis is discussed below (“Effective heat of formation model” section) in detail. Further discourse concerns experimental and theoretical studies of the physical properties for only two phases obtained by this method, namely  $\text{Mn}_4\text{Si}_7$  and  $\text{Mn}_{17}\text{Si}_{30}$ .

The  $\text{Mn}_4\text{Si}_7$  and  $\text{Mn}_{17}\text{Si}_{30}$  thin films were formed on  $1^\circ$ -miscut vicinal p-Si(100) substrate ( $\rho \sim 5$ – $10 \Omega \text{ cm}$ ) at 630 °C by solid-state reaction method in ultrahigh vacuum chamber equipped with reflection high energy diffraction (RHEED) unit [30]. Before growth, Si substrate was chemically cleaned and etched [31]. Si substrate was exposed to a gradual thermal treatment for 3 h to 650 °C at a rate of 4 °C/min in UHV (base pressure  $6.5 \times 10^{-8} \text{ Pa}$ ). The wafer was flashed at 850–900 °C until well-ordered ( $2 \times 1$ ) reconstruction was detected by RHEED, evidencing formation of the atomically clean silicon surface. After the specimen was cooled down to the room temperature, Mn and Si were deposited via thermal evaporation from Knudsen cells onto the silicon substrate surface.

Manganese and silicon deposition was divided into either three ( $\text{Mn}_{17}\text{Si}_{30}$ ) or four ( $\text{Mn}_4\text{Si}_7$ ) stages. The first stage was the same for both resultant compounds. During this stage, a 15-nm-thick layer of manganese was deposited. Then, a gradient layer of Mn–Si was created, where the Si/Mn layer ratio varied linearly either from 0.85 (Si = 35 at.%) to 2.86 (Si = 63.6 at.%) or from 0.45 (Si = 21 at.%) to 0.85 (Si = 35 at.%) for  $\text{Mn}_4\text{Si}_7$  and  $\text{Mn}_{17}\text{Si}_{30}$  resultant films, respectively. Manganese deposition rate was constant at 0.51 nm/min, and the silicon rate was increased from 0.2 to 1.46 nm/min ( $\text{Mn}_4\text{Si}_7$  sample), 0.2–0.41 nm/min ( $\text{Mn}_{17}\text{Si}_{30}$  sample) during 11 min. The third stage, in case of the  $\text{Mn}_4\text{Si}_7$  resultant thin film, was the formation of the top layer consisted of manganese-silicon mixture under the constant Si/Mn deposition rate ratio of 2.86 during 17 min, while the  $\text{Mn}_{17}\text{Si}_{30}$  technology procedure had no the top layer formation. A schematic illustration of the initial layer stacks is depicted below in “Effective heat of

formation model” section. The final stage of the synthesis was annealing of the Mn–Si layer stack at a temperature of 600 °C for 1 h.

Powder X-ray diffraction (PXRD) investigations were performed on a PANalytical X'Pert Pro MPD diffractometer with a PIXcel detector and a secondary graphite monochromator on Cu K $\alpha$  radiation. The PXRD patterns were collected in the angular range from 24° to 56° 2 $\theta$ . The full-profile refinement of crystal structures was carried out using the derivative difference minimisation (DDM) method [32] taking into account the film thickness effect and the preferred orientation of crystallites. Morphology characteristic examination of the samples was performed by transmission electron microscopy (TEM) on Hitachi HT7700 microscope equipped with ED spectrometer 6T/60 Bruker. X-ray photoelectron spectroscopy methods were applied to examine electronic structure of the HMS films. Photoemission spectra were measured using K-Alpha+™ XPS system (Thermo Fisher Scientific, USA). X-ray power load (monochromated Al K-alpha) was 60 W at the spot size 400  $\mu$ m; an ambient vacuum was better than 10<sup>-6</sup> Pa. The electron energy analyser was operated with a pass energy of 10 eV for the core level and 20 eV for the valence band mapping modes. The step size of 0.05 eV was employed, and each peak was scanned up to 1000 times to achieve desirable signal-to-noise ratio. To remove surface contamination, the sputtering using Ar + ion bombardment (500 eV, 50 s.) was used. The presence of oxygen on the surface during the experiments was monitored by measuring the intensity of the 1s oxygen line in the spectra before and after the experiment. The energy calibration during each cycle of the measurements has been performed using the 4f states of an Au foil kept in contact with the analysed sample. All the measurements were taken at room temperature. Photon energy dependence of the relative permittivity is calculated from the reflectance and transmittance spectra within the Drude–Lorentz model. In the calculations, we used the optical model involving a homogeneous isotropic film with a thickness determined by TEM and unknown relative permittivity on isotropic Si substrate with known optical characteristics. Reflectance spectra measurements were taken on Agilent Cary 5000 in wide spectral range  $E = 0.75$ –6.5 eV. For investigation of optical features caused by degeneracy and crystal structure defects, the low-energy range of transmittance spectra was investigated by both Shimadzu UV-

3600 spectrophotometer and Bruker Vertex 80 vacuum FT-IR spectrometer in the range of 0.076–1 eV. Transport properties (resistance and Hall effect) were examined in the temperature range from 4.2 to 300 K and magnetic field of 1 T by four probe Van der Pauw technique with the help of cryogenic probe station Lakeshore EMPX-HF 2 and homebuilt facility [31] based on a helium cryostat and KEITHLEY-2400 current/voltage source meter.

## Results and discussion

### Effective heat of formation model

Effective heat of formation (EHF) model allows one to predict a phase formation during solid phase reaction, reactive deposition and other thin film creation methods [33, 34]. The EHF model implies that standard heat of formation  $\Delta H^\circ$  of any compound or alloy of metal–semiconductor or the metal–metal system can be indicative how the free energy  $\Delta G^\circ$  changes during the solid-state reaction. The formation of a specific phase with the most negative heat of formation will lead to the biggest free energy change [34]. In brief, the first phase to form in the reaction occurring at a metal–silicon interface in solid is a congruently melting phase with the most negative heat of formation at the concentration of liquidus minimum of the binary system. The chemical composition at liquidus minimum is chosen as the effective concentration during the solid-state reaction at the interface between two solids due to the higher atomic mobility at this point [34]. It is clear that except for atomic mobility, many other factors can govern the solid-state reaction. Impurities, diffusion barriers, lattice-mismatch-induced stress can affect the actual quantity of reactants available at the interface. However, the approach described above, as many authors showed, is usually correct for prediction of phase formation sequence. Thus, liquidus minimum composition is taken to estimate the heat of formation as function of concentration by the equation,

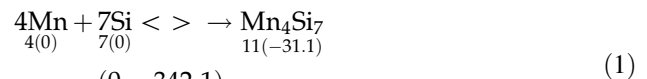
$$\Delta H' = \Delta H^\circ \times \frac{\text{Effective concentration limiting element}}{\text{Compound concentration limiting element}}$$

where  $\Delta H'$  (effective heat of formation) and  $\Delta H^\circ$  are expressed in kJ per mole of atoms. It is asserted that room temperature value of the heat of formation is suitable for practical usage in thermodynamic

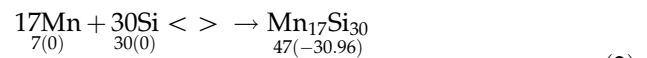
calculations at any temperature [34]. According to the phase diagram of Mn–Si system (Fig. 1), MnSi and Mn<sub>5</sub>Si<sub>3</sub> are the only phases, which melt congruently. The lowest liquidus point at  $T = 1040\text{ }^{\circ}\text{C}$  defines the effective concentration of silicon as 20 at.%. Consequently, Mn<sub>5</sub>Si<sub>3</sub> is regarded as first phase for formation due to higher value of effective heat for formation,  $-18\text{ kJ/mol at.}$ , whereas  $\Delta H'$  for MnSi equals to  $-15.8\text{ kJ/mol at.}$  (Fig. 1). The effective heat of formation ( $\Delta H'$ ) diagram was calculated with help of heat of formation obtained by Berche et al. [35] using ab initio methods. However, examination of phase formation sequence in a pure Mn thin film on a silicon substrate shows that the MnSi is the first phase to form during

Mn–Si solid-state reactions. Mn<sub>5</sub>Si<sub>3</sub> unit cell has 16 atoms per unit cell, and MnSi (B20 type) has only 8 atoms, which makes it easier to nucleate. Usually, the greater value of atoms per compound unit cell is considered as a significant factor to change the first phase in the phase formation sequence [34]. However, taking into account a possible error in heat of formation estimation at 10% the difference between the heat of formation can be as low as 0.1% and, as a result, two times lesser number of atoms per the MnSi unit cell gives an advance for priority in phase formation sequence. After the whole amount of available Mn atoms are used for formation of the MnSi layer on bulk silicon, the next phase for formation at higher temperature is a phase on the diagram of effective heat of formation  $\Delta H'$  located towards silicon enrichment, i.e. higher manganese silicide. The difference in the heat of formation between various higher manganese silicides is expected to be very small due to similarity of the compounds. Thus, it seems to be not possible to predict which phase of HMS family will form in MnSi/Si heterostructure with further temperature increase.

Nevertheless, one can imagine a situation where the initial system for further formation of HMS compounds is not only MnSi and contains other Mn-rich silicides, and even can exclude MnSi phase. Thus, by varying the set of initial compounds, it is possible to indicate by calculating the heat of reaction  $\Delta H_R$  whether a reaction is thermodynamically possible or not, and for which HMS compound it is more favourable. Whereas the heat of formation expressed in kJ/mol at for HMS compound is expected to be very similar, conversely the heat of reaction corresponded to Avogadro’s number of particular HMS phase “molecules” shows a significant difference. For instance,  $\Delta H'$  for Mn<sub>4</sub>Si<sub>7</sub> equals to 342.1 kJ/mol (1), for Mn<sub>17</sub>Si<sub>30</sub>—1455.12 kJ/mol (2). Their heats of reaction  $\Delta H_R$  are calculated as follows:

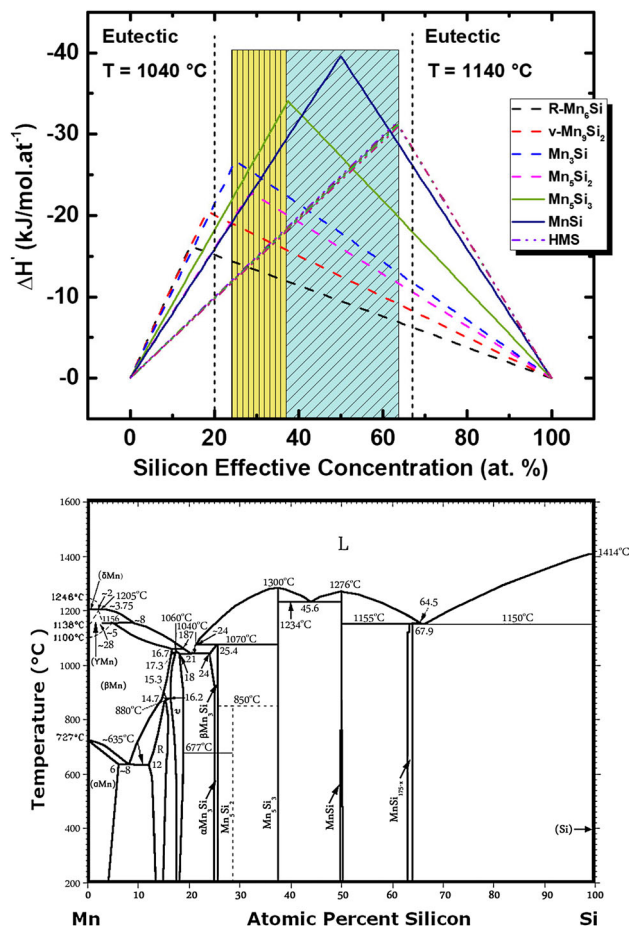


$$\Delta H_R^{\circ} = \frac{(0 - 342.1)}{11} = -31.1\text{ kJ}(\text{mol at})^{-1}$$



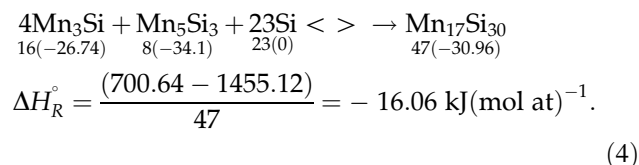
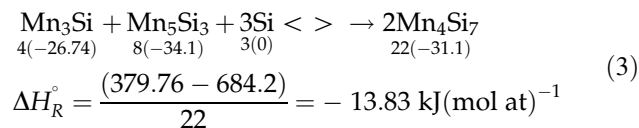
$$\Delta H_R^{\circ} = \frac{(0 - 1455.12)}{47} = -30.96\text{ kJ}(\text{mol at})^{-1}$$

Numbers in parentheses beneath the reactants correspond to the heats of formation of the reactants. One can easily see that effective heat of reaction in (1)



**Figure 1** Effective heat of formation ( $\Delta H'$ ) diagram for compound phase formation top and phase diagram bottom for the Mn–Si system [36]. Dashed triangles indicate noncongruently melting phases, as they have difficulty in nucleating in the case of the silicides. At the composition of the liquidus minimum, it can be seen that the phase Mn<sub>5</sub>Si<sub>3</sub> has the most negative effective heat of formation and therefore is predicted to form first.

and (2), in both cases, is almost the same. The reason for the slight difference is because we took the value of the heat of formation for HMS compounds by approximation of the curve reported in [35]. Then, if we consider the system as follows:



The heat of reaction in case of  $\text{Mn}_4\text{Si}_7$  (3) is less than in the  $\text{Mn}_{17}\text{Si}_{30}$  reaction (4). Therefore, the  $\text{Mn}_{17}\text{Si}_{30}$  reaction is thermodynamically more favourable. The initial system considered above implies that  $\text{Mn}_{17}\text{Si}_{30}$  phase is more possible to form than  $\text{Mn}_4\text{Si}_7$  compound. Hence, by varying the set of initial phases for further formation of some higher manganese silicide or another one could determine an initial reactant combination, which is the most favourable to create a particular HMS compound, if such combination exists. Table 1 contains some chosen results of the calculation of the heats of reaction ( $\Delta H_R^\circ$ ) for the interaction of  $\text{Mn}_3\text{Si}$ ,  $\text{MnSi}$ ,  $\text{Mn}_5\text{Si}_3$ ,  $\text{Mn}_9\text{Si}_2$ ,  $\text{R-Mn}_6\text{Si}$  phases with silicon to form different higher manganese silicides. It is clear that the most negative heat of reaction will be observed when reactants are only Si and Mn, but here we consider the situation when one or another manganese silicide phase is obligatorily involved to the formation of a higher manganese silicide. We suppose in the calculation that silicon is available without limits from the substrate. First row with the results depicts which initial reactant combination gives rise to the biggest free energy change. The most negative value corresponds to  $\text{Mn}_{39}\text{Si}_{68}$  because of more bonding between Mn and Si are created for forming  $\text{Mn}_{39}\text{Si}_{68}$  equal to Avogadro's number. Maximum of the heat of reaction for different HMS phases, as it can be seen, is observed for different initial reactants combination.  $\text{Mn}_{17}\text{Si}_{30}$  compound formation is most negative when only  $\text{R-Mn}_6\text{Si}$  is present along with silicon. The heat of reaction maximum for other HMS compounds requires that  $\text{R-Mn}_6\text{Si}$  should be coupled with  $\text{Mn}_3\text{Si}$  or  $\text{MnSi}$  silicides. In Table 1 one can see the heat of reaction maximum calculated for the case when the

reaction product with a composition lying outside the range of composition of the reactants is not taken into account. In other words after higher manganese silicide "molecules" are created so that their total quantity is equal to Avogadro's number no manganese is available for the further reaction. The initial combination of the reactants has changed for the  $\text{Mn}_{11}\text{Si}_{19}$ ,  $\text{Mn}_{26}\text{Si}_{45}$ ,  $\text{Mn}_4\text{Si}_7$  and  $\text{Mn}_{17}\text{Si}_{30}$  compounds, while the most negative heat of reaction still corresponds to  $\text{Mn}_{39}\text{Si}_{68}$  phase. A situation when manganese atoms no longer available for the reaction should prevent further formation of HMS divergent compound. Thus, by introducing restriction on the obligatory presence or absence of some manganese silicide or other phase we found conditions when  $\text{Mn}_{17}\text{Si}_{30}$  phase has one of the most negative heats of reaction in comparison with other HMS compounds. The initial combination of reactants was such that the presence of  $\text{Mn}_3\text{Si}$  and  $\text{Mn}_5\text{Si}_3$  phases was obligatory and other non-HMS compounds were excluded. One can see that the reactions with excess of manganese (depicted with red and italic font) show the highest heat of reaction. In case of  $\text{Mn}_4\text{Si}_7$   $\Delta H_R^\circ$  turns to be positive. The  $\text{Mn}_{26}\text{Si}_{45}$  compound has close value of the heat of reaction to  $\text{Mn}_{17}\text{Si}_{30}$  ( $-16.9$  and  $-16.1$ , respectively) and is considered as thermodynamically possible to form from the interaction of  $\text{Mn}_3\text{Si}$  and  $\text{Mn}_5\text{Si}_3$  with silicon, along with  $\text{Mn}_{17}\text{Si}_{30}$  compound. As an example, we added the heat of reaction maximum data where  $\text{Mn}_3\text{Si}$  and  $\text{MnSi}$  phases were obligatory and other non-HMS compounds were excluded. As a result, the most negative heat of reaction is now for  $\text{Mn}_{19}\text{Si}_{33}$  phase, when the values for  $\text{Mn}_4\text{Si}_7$  and  $\text{Mn}_{17}\text{Si}_{30}$  have changed slightly.

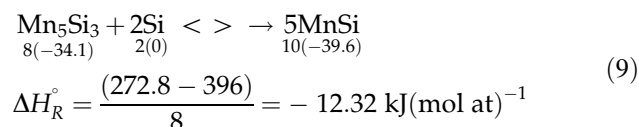
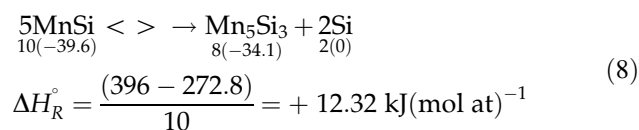
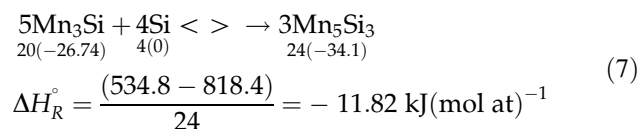
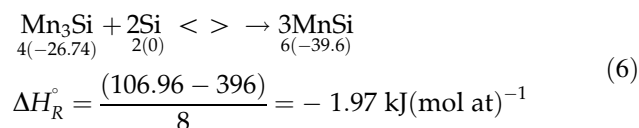
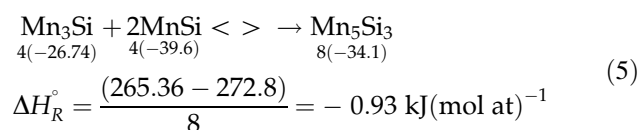
Thus, we suggest that thermal annealing of a composite film composed of  $\text{Mn}_3\text{Si}$  and  $\text{Mn}_5\text{Si}_3$  mixture on silicon substrate could result in the formation of  $\text{Mn}_{17}\text{Si}_{30}$  or  $\text{Mn}_{26}\text{Si}_{45}$  compounds. As we considered above the first phase to form during thermal annealing of pure Mn layer is  $\text{MnSi}$  due to effective concentration on the manganese-silicon interface, effective heat of formation and simplicity of  $\text{MnSi}$  (B20 type) unit cell [34]. This assertion is confirmed by experimental findings in several works [37, 38]. The phase formation activation temperature is around  $400^\circ\text{C}$ . A uniform layer of  $\text{MnSi}$  appears after a rise of the temperature up to  $500^\circ\text{C}$ . In turn,  $\text{Mn}_3\text{Si}$  grows when there is a diffusion barrier (thin silicon dioxide) between the silicon substrate and pure Mn

**Table 1** Calculated heats of reaction ( $\Delta H_R^0$ ) for the interaction of  $Mn_3Si$ ,  $MnSi$ ,  $Mn_5Si_3$ ,  $Mn_9Si_2$ ,  $R-Mn_6Si$  with silicon to form one formula unit of different higher manganese silicides (see comments in the text)

Phase	$Mn_7Si_{12}$	$Mn_{11}Si_{19}$	$Mn_{26}Si_{45}$	$Mn_{15}Si_{26}$	$Mn_{19}Si_{33}$	$Mn_{27}Si_{47}$	$Mn_{39}Si_{68}$	$Mn_4Si_7$	$Mn_{17}Si_{30}$	Restrictions									
Si/Mn	1.714	1.727	1.731	1.733	1.737	1.741	1.744	1.75	1.765										
VEC	13.86	13.91	13.92	13.93	13.95	13.96	13.97	14	14.06										
Heat of reaction maximum ( $\Delta H_R^0$ )																			
$Mn_3Si$	0	-21.3	0	-23.0	1	-23.1	0	-23.1	1	-23.6	1	-23.8	0	-17.6	0	-23.2	<i>No</i>		
$MnSi$	1	0	0	0	0	0	1	0	0	0	0	0	0	0	0	0			
$Mn_5Si_3$	0	0	0	0	0	0	0	0	0	0	0	0	0	0	0	0			
Si	10	17	40	23	29	42	29	42	61	61	61	61	6	27	27	27			
$Mn_9Si_2$	0	0	0	0	0	0	0	0	0	0	0	0	0	0	0	0			
$R-Mn_6Si$	1	2	4	2	3	4	3	4	6	6	6	6	1	3	3	3			
Heat of reaction maximum ( $\Delta H_R^0$ ) when there is no Mn at the exit of the reaction																			
$Mn_3Si$	0	-21.3	1	-18.7	0	-22.6	1	-23.1	0	-23.1	1	-23.6	1	-23.8	1	-14.2	1	-20.5	<i>No</i>
$MnSi$	1	2	2	0	0	0	1	0	0	0	0	0	0	0	0	1	2	0	
$Mn_5Si_3$	0	0	0	0	0	0	0	0	0	0	0	0	0	0	0	0	0	0	
Si	10	15	39	23	29	42	29	42	61	61	61	61	5	25	25	25	25	25	
$Mn_9Si_2$	0	0	0	0	0	0	0	0	0	0	0	0	0	0	0	0	0	0	
$R-Mn_6Si$	1	1	4	2	3	4	3	4	6	6	6	6	0	2	0	2	4	4	<i>On</i>
$Mn_3Si$	1	-10.9	2	-15.1	7	-16.9	4	-13.5	3	-14.6	4	-14.4	8	-15.5	1	2.51	4	-16.1	<i>On</i>
$MnSi$	0	-	-	-	0	0	0	-	-	-	-	-	0	0	0	0	-	-	$Mn_3Si_3$
$Mn_5Si_3$	1	1	1	1	2	3	2	1	2	3	3	3	1	1	1	1	1	1	$Mn_5Si_3$
Si	8	14	35	19	24	34	24	34	51	51	51	51	3	23	3	23	23	23	<i>Off</i>
$Mn_9Si_2$	0	-	-	0	-	-	0	-	-	-	-	-	0	0	0	0	-	-	<i>Others</i>
$R-Mn_6Si$	0	-	-	0	-	-	0	-	-	-	-	-	0	0	0	0	-	-	<i>Others</i>
$Mn_3Si$	2	-16.0	3	-15.3	8	-17.0	4	-15.0	6	-17.4	8	-16.4	12	-16.9	1	-14.2	5	-16.2	<i>On</i>
$MnSi$	1	2	2	3	1	3	1	3	3	3	3	3	1	1	1	1	2	2	$Mn_3Si_3$
$Mn_5Si_3$	-	-	-	-	-	-	-	-	-	-	-	-	-	-	-	-	-	-	<i>Off</i>
Si	9	14	35	19	26	36	26	36	53	53	53	53	5	23	5	23	23	23	<i>Off</i>
$Mn_9Si_2$	-	-	-	-	-	-	-	-	-	-	-	-	-	-	-	-	-	-	<i>Others</i>
$R-Mn_6Si$	-	-	-	-	-	-	-	-	-	-	-	-	-	-	-	-	-	-	<i>Others</i>

Numbers in the rows correspond to the quantity of formula units of the reactants used to calculate  $\Delta H_R^0$

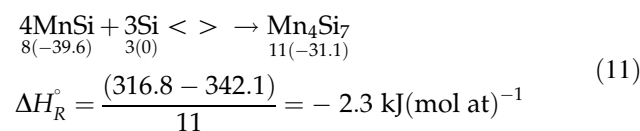
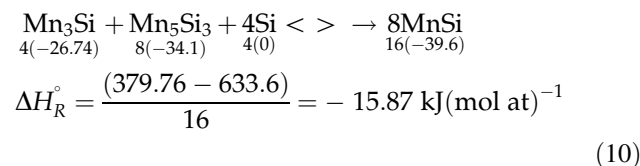
layer at 380–430 °C. Hence, the initiation of Mn<sub>3</sub>Si could be done by changing effective concentration reaction layer artificially by creation amorphous Mn–Si layer with the composition of 3:1 on the top the manganese layer, which may play a role of the diffusion barrier for silicon atoms from the substrate. At the temperature considered (~ 400 °C) such silicon diffusion process will initiate a formation of MnSi phase and silicon atoms coming from the substrate will be consumed for a MnSi formation, while the top layer starts to transform into Mn<sub>3</sub>Si compound. Further annealing under given temperature should result in the formation of the Mn<sub>5</sub>Si<sub>3</sub> layer due to high diffusion of silicon through the MnSi layer [39]. It can be seen that formation of Mn<sub>5</sub>Si<sub>3</sub> from Mn<sub>3</sub>Si and MnSi (5) is thermodynamically less favourable than in case of the reaction (6). Formation of Mn<sub>5</sub>Si<sub>3</sub> from MnSi is thermodynamically forbidden (8). Thus, all Mn<sub>3</sub>Si layer should transform to Mn<sub>5</sub>Si<sub>3</sub> (7), and after that, the formation of MnSi will follow as it prescribed by reaction (9).



Nevertheless, we suppose that simultaneous coexistence of Mn<sub>3</sub>Si and Mn<sub>5</sub>Si<sub>3</sub> as a mixture in one layer and a further rapid temperature rising to the activation temperature of the higher manganese silicide nucleation will force to skip the formation of MnSi compound. Even though the formation of MnSi according to the reaction (10) is thermodynamically possible, we expect that formation of MnSi will give

way to HMS phase due higher temperature and high diffusivity of silicon through MnSi layer.

A Mn<sub>3</sub>Si and Mn<sub>5</sub>Si<sub>3</sub> mixture layer, as we presume, could be created by the preliminary formation of amorphous Mn–Si gradient layer on the top of pure manganese layer lying on the Si substrate surface (Fig. 2).



Composition range of the gradient layer should correspond to the region on effective heat diagram where the most negative effective heat of formation is for Mn<sub>3</sub>Si and Mn<sub>5</sub>Si<sub>3</sub> phases (Fig. 1 yellow area). A possible lack of manganese for the formation will be accomplished by diffusion of manganese from the Mn bottom layer. It can be seen that formation of HMS compound from MnSi (11) is thermodynamically less favourable than its formation from the mixture of Mn<sub>3</sub>Si and Mn<sub>5</sub>Si<sub>3</sub> (4). Thus, after the top mixture layer will be transformed into HMS compound formation of HMS from MnSi should start. The two reactants atomically mix in the reaction region, and then these atoms are rearranged on the lattice of the growing phase, which we suppose should be Mn<sub>17</sub>Si<sub>30</sub> or Mn<sub>26</sub>Si<sub>45</sub>. Conversely, if one place the amorphous gradient layer with silicon content from 35 up to 63.6 at.% (Fig. 1 light blue area) and then on the top of the gradient layer, a layer with HMS stoichiometry the phase formation sequence is expected to change (Fig. 2 right). Mn and Si in the top and gradient layer at temperatures below the HMS formation will tend to form MnSi compound and only at the interface between the gradient layer and pure manganese layer the possibility of forming manganese-rich phases will exist. It is expected that formation of HMS layer at elevated temperature will be carried out easier inside the top layer because the necessary quantity of silicon atoms already exists in the layer. Thus, there is no need for an HMS nucleation to wait for silicon atoms diffusing through the bottom MnSi layer. Moreover, HMS formation may start even under lower temperature (300 °C) when



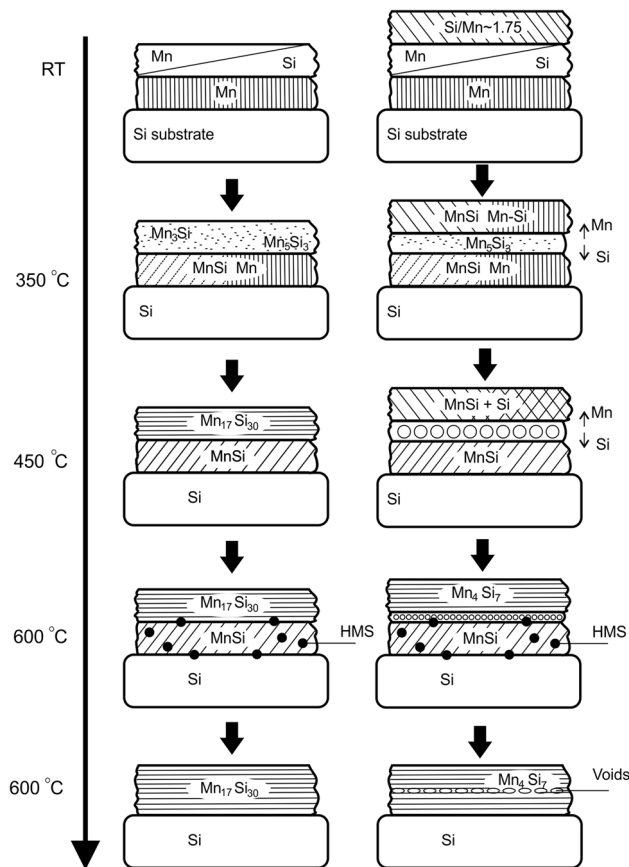
the chemical composition is equal to that of HMS compounds [40]. Thus, there should be two reaction fronts of HMS nucleation in the top of the layer stack and at the bottom, inside the MnSi layer. The bottom reaction is expected to be less favourable due to the low negative heat of reaction (11). The samples in this work were prepared following the logic discussed above (Fig. 2).

### Structural properties characterisation

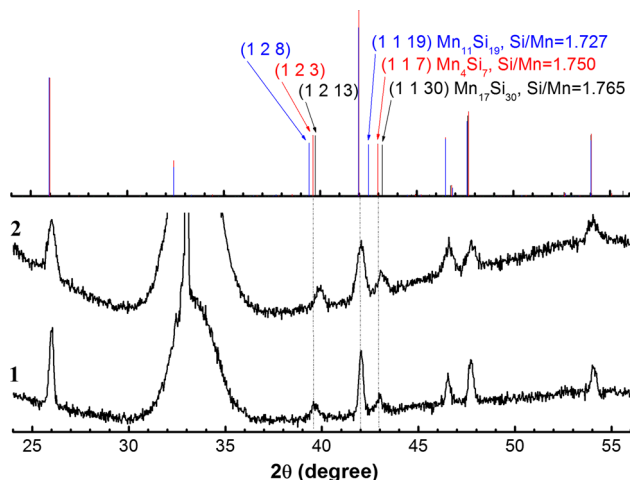
Recorded PXRD patterns for the  $Mn_4Si_7$  and  $Mn_{17}Si_{30}$  samples are shown in comparison with the simulated ones for different manganese silicide phases in Fig. 3. The most structure-sensitive reflections of the Nowotny chimney-ladder phases  $Mn_mSi_n$  are those with the Miller indexes (1 2 n-m) and (1 1 m), whose positions are regularly shifted to the smaller d-spacing (or higher  $2\theta$ ) with the Si/Mn ratio increase. The respective peak positions for the sample 1 corresponded well to the  $Mn_4Si_7$  phase with the known

crystal structure. Its tetragonal ( $P-4c2$ ) lattice parameters were successfully refined by the DDM method to the values of  $a = b = 5.519(1)$  and  $c = 17.466(3)$  Å. In the PXRD pattern of sample 2, the structure-sensitive peak positions were notably shifted to the higher  $2\theta$  angles (Fig. 3), pointing to a higher Si/Mn ratio. Among the known, structurally characterised chimney-ladder  $Mn_mSi_n$  phase,  $Mn_4Si_7$  has the biggest Si/Mn ratio of 1.75. In the (Mn, Cr) $_mSi_n$  system, however, a  $(Mn_{0.75}Cr_{0.25})_{17}Si_{30}$  phase was described [24] with a larger Si/metal ratio of 1.765. Idealised coordinates of Mn and Si atoms in the tetragonal ( $I-42d$ ) crystal lattice were calculated geometrically and then optimised using the DFT energy minimisation approach (see Supplementary, Table S1) to check the applicability of this structure type to the description of  $Mn_mSi_n$  phase in sample 2. The full-profile DDM structure refinement using the DFT optimised (and fixed) atomic coordinates for the sample 2 resulted in a good agreement between the observed and calculated PXRD patterns (Fig. 4) and gave the tetragonal ( $I-42d$ ) lattice parameters  $a = b = 5.518(2)$  and  $c = 74.31(3)$  Å. Below sample 1 is marked as  $Mn_4Si_7$ , and sample 2—as  $Mn_{17}Si_{30}$ .

Figure 5 represents transmission electron microscopy images of the samples, obtained in a cross-sectional geometry. The average interplanar distance value for the sample  $Mn_4Si_7$  is 4.64 Å (Fig. 5b) which corresponded to (012) interplanar distance (4.68 Å [41]). In case of  $Mn_{17}Si_{30}$  the planes observed are separated by 4.14 Å (Fig. 5d) which can correspond to (1 0 11) plane. The average film thicknesses are estimated as 24 and 18 nm for  $Mn_4Si_7$  and  $Mn_{17}Si_{30}$  samples, respectively. The films obtained are not flat, and the thickness can vary from 23 nm up to 48 nm ( $Mn_4Si_7$ ) in some places detected over the whole lamella prepared for TEM studies. In case of the  $Mn_{17}Si_{30}$  sample, the variation of thickness lies in the range between 17 and 23 nm. Thus, we conclude that thickness spreads are about 0.7 and 0.3 for  $Mn_4Si_7$  and  $Mn_{17}Si_{30}$  samples, respectively. It can be easily seen that  $Mn_{17}Si_{30}$  film is homogeneous over the whole thickness, whereas on the TEM image of the  $Mn_4Si_7$  sample one can easily distinguish two layers separated by a thin sublayer with higher contrast. According to the XRD analysis,  $Mn_4Si_7$  sample is monophasic. The electron diffraction analysis, which is more sensitive in case of nanostructures, was made with the help of electron diffraction analysis software developed by Klinger [42]. The complicity of HMS

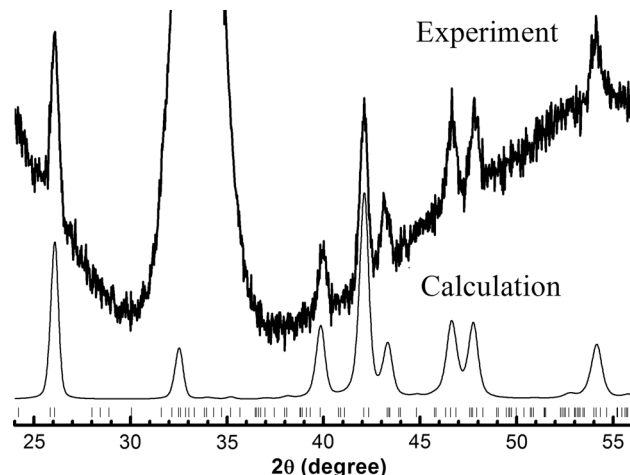


**Figure 2** Schematic illustration of the synthesis procedure for left:  $Mn_{17}Si_{30}$  and right  $Mn_4Si_7$  sample.



**Figure 3** Top: calculated PXR D patterns for three  $Mn_mSi_n$  phases with different Si/Mn ratios. Bottom: experimental PXR D patterns of the  $Mn_4Si_7$  (1) and  $Mn_{17}Si_{30}$  (2) samples. Arrows point to the most structure-sensitive reflections with their Miller indices given in the brackets.

structure and variety of the spotty rings resulted from its structure does not allow us to reveal a presence of other Mn–Si phases (Supplementary Fig. S1). Hence, we suppose that this intermediate high-contrast layer is formed from voids or silicon inclusions. They could appear when the bottom reaction layer reached the earlier formed the  $Mn_4Si_7$  top layer. Such nanopores or inclusions of other compounds could be used to tune thermal conductivity through phonon scattering for increasing thermoelectric performance [43, 44]. Magnified view of  $Mn_4Si_7$  cross section reveals that  $Mn_4Si_7$  compound in the bottom and upper layers have the same orientation. Atomic planes spread over the whole film thickness without changing their direction (Fig. 5d). Thus, the voids do not form a continuous layer. On both TEM images ( $Mn_4Si_7$  and  $Mn_{17}Si_{30}$ ) the wave-like interface with silicon is observed. Such interface is supposed to be due to reaction front propagation towards the silicon substrate. It is known that transformation of MnSi into HMS compounds at elevated temperatures 485–600 °C occurs in three dimensions in patches inside the MnSi layer. In a situation when the HMS layer already exists, such transformation could proceed faster in the vicinity of the HMS layer due to orienting influence of presented HMS crystal structure. Atoms are rearranged to the lattice of upper HMS layer easier than in the case when orienting HMS phase is absent. The reactant atoms then need more time to create an island with the critical



**Figure 4** Observed and calculated PXR D profiles for sample 2 after DDM refinement.

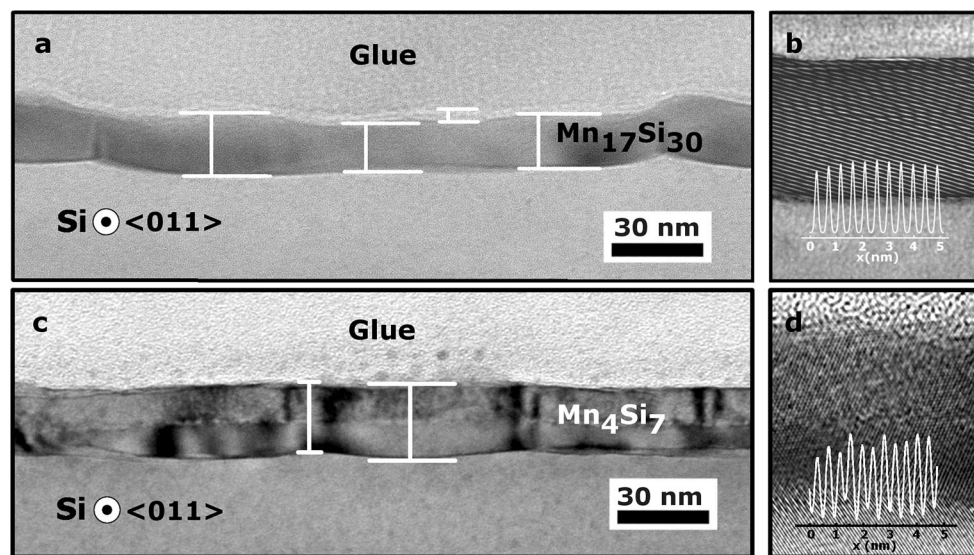
size. A schematic picture of phase formation sequence according to structural analysis and EHF model is given in Fig. 2.

Figure 6 demonstrates the TEM planar view of the samples obtained. Different initial layer stack architecture resulted not only in the formation of different HMS compounds, but it also caused the appearance of drastically different typical crystallites forms and sizes. The  $Mn_{17}Si_{30}$  film consists of larger crystallites of an elongated shape with preferentially convex borders, about 1  $\mu\text{m}$  length and 0.25  $\mu\text{m}$  width (Fig. 6b), whereas the  $Mn_4Si_7$  phase film is packed with smaller crystallites. The typical lateral size of  $Mn_4Si_7$  crystallites varies in the range of 50 nm up to 500 nm. Grain borders have preferentially concave shapes (Fig. 6a). This property can positively affect the thermoelectric efficiency of this film. Therefore, the thermal conductivity in the direction perpendicular to the preferential orientation of the crystallites will be decreased due to the scattering of phonons at the interface of the crystallites. Moreover, the  $Mn_4Si_7$  sample contains small inclusions with the higher contrast depicted with blue lines. Such phenomenon can be due to the void inclusions in  $Mn_4Si_7$ /Si lamella prepared for TEM studies. The electron loss in such areas will be smaller than in areas composed of  $Mn_4Si_7$  and silicon substrate thereby ensuring higher contrast.

## Transport properties

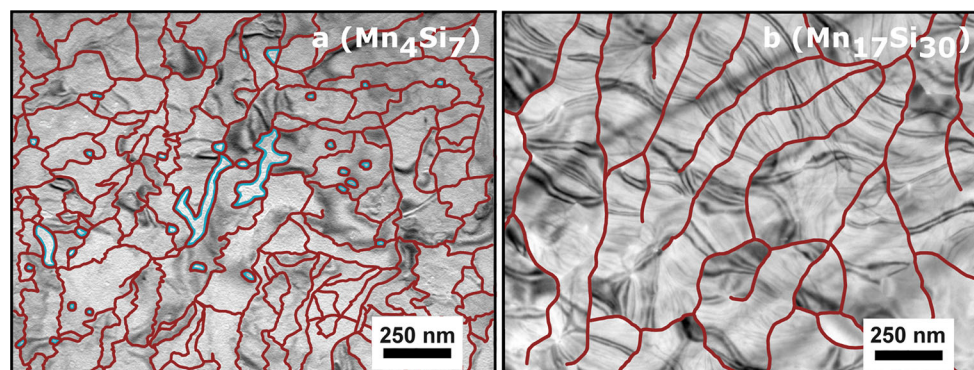
For both samples, the standard Hall effect was measured to determine the concentration ( $p$ ), and Hall mobility of the charge carriers ( $\mu_H$ ), which were calculated using the values of resistivity for certain temperature and magnitude of the Hall voltage at magnetic field of 1T. Temperature dependence of the resistivity for two samples is shown in Fig. 7. One can easily see a knee situated around 200 K, denoted with the red vertical line. It may be interpreted as current channel switching. Above 200 K silicon substrate has lower or comparable resistivity with respect to the thin films, and the electrical current is shunted by Si bulk and flows through silicon substrate. That is why

the resistance behaves similarly above 200 K. This phenomenon is observed in different conductive films such as  $\text{Fe}_3\text{Si}$  [31],  $\text{Cu}_{80}\text{Co}_{20}$  [45],  $\text{Fe}_2\text{SiO}_4$  and in many other ones deposited on silicon substrates [46]. The conducting channel switching temperature may depend on bias current, doping concentration, thin film resistivity, and the presence of interface layer. While above the crossover temperature,  $\sim 200$  K, behaviour of resistivity is similar in each material; below the crossover, the resistivity behaviour becomes different. A small increase (by  $\sim 2.5$  times) in the  $\text{Mn}_4\text{Si}_7$  resistivity is observed over the whole temperature region. The resistivity change in the low-temperature region (4–25 K) is not such significant, as it should be in a non-generated semiconductor. It

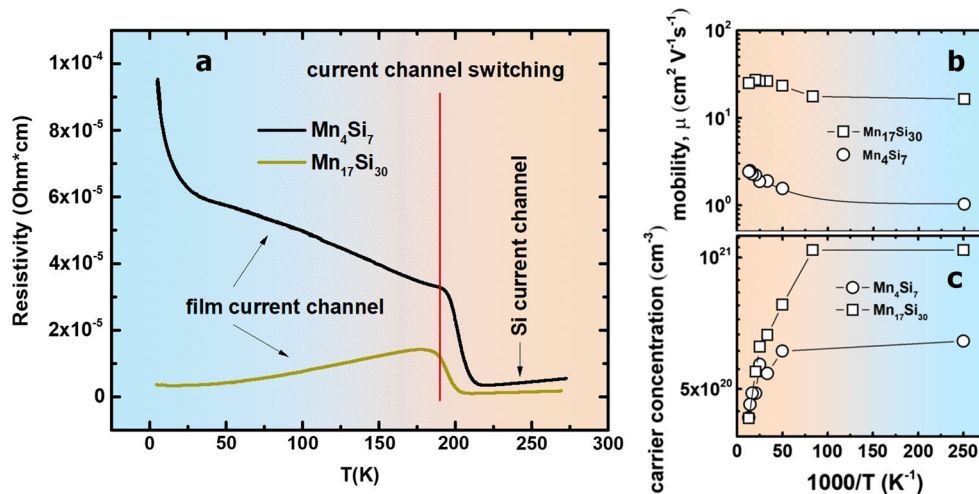


**Figure 5** Transmission electron microscopy images; cross section of **a**  $\text{Mn}_{17}\text{Si}_{30}$ , **b** magnified view of  $\text{Mn}_{17}\text{Si}_{30}$  film with inset representing interplanar distances between 11 planes; average

interplanar distance value is 4.64 Å, **c**  $\text{Mn}_4\text{Si}_7$  cross-sectional view, **d** magnified view of  $\text{Mn}_4\text{Si}_7$ —average interplanar distance value is 4.14 Å.



**Figure 6** Transmission electron microscopy images; planar view **a**  $\text{Mn}_4\text{Si}_7$ , **b**  $\text{Mn}_{17}\text{Si}_{30}$ ; red lines represent crystallite borders; blue depict areas with high-intensity contrast.



**Figure 7** Transport characteristics of the  $\text{Mn}_4\text{Si}_7$  and  $\text{Mn}_{17}\text{Si}_{30}$  polycrystalline films **a** temperature dependence of the resistivity, **b** mobility, **c** carrier concentration at a current  $I = 100$  mA.

increases by only 1.5 times, whereas in case of silicon it raises up by two orders of magnitude due to the carriers freezing out. For  $\text{Mn}_{17}\text{Si}_{30}$ , we observe a decrease in resistivity upon cooling, which corresponds to the metallic type of conductivity. Thus, we suppose that both samples are p-type degenerated semiconductors in the 4–77 K range. Resistivity values at the crossover point (180 K) are 1.4 and  $3.3 \times 10^{-3} \Omega \text{ cm}$  for  $\text{Mn}_{17}\text{Si}_{30}$  and  $\text{Mn}_4\text{Si}_7$ , respectively. These values are comparable with the data reported earlier for various HMS,  $\rho = 1.1 \times 10^{-3}$  [47],  $1.6 \times 10^{-3}$  [48], 1.78–2.1  $\Omega \text{ cm}$  [49] at room temperature.

Figure 7b shows the temperature dependence of Hall mobility of the HMS samples. The mobility in  $\text{Mn}_4\text{Si}_7$  and  $\text{Mn}_{17}\text{Si}_{30}$  is weakly dependent on the temperature, which can be referred to their degenerate nature. At  $T = 77$  K the mobility of the  $\text{Mn}_4\text{Si}_7$  and  $\text{Mn}_{17}\text{Si}_{30}$  phases differs by one order of magnitude, 2.5 and 25  $\text{cm}^2/\text{V s}$ , respectively. Migas et al. [13] earlier considered the mobility of perfect and defect  $\text{Mn}_4\text{Si}_7$  crystal from the theoretical point of view. The values obtained at  $T = 77$  K must lie around 4 and 1.8  $\text{cm}^2/\text{V s}$  for neutral impurities concentration of  $10^{18}$  and  $10^{20} \text{ cm}^{-3}$  in the  $\text{Mn}_4\text{Si}_7$  compound, respectively. The experimental value obtained for  $\text{Mn}_4\text{Si}_7$  is 2.5  $\text{cm}^2/\text{V s}$  that is in good agreement with data obtained by Migas et al. [13]. However, the Hall mobility for  $\text{Mn}_{17}\text{Si}_{30}$  compound (25  $\text{cm}^2/\text{V s}$ ) is out of the mobility value range reported earlier – 0.06 [47], 2.14 [48], 1.92–2.07  $\text{cm}^2/\text{V s}$  [49] at room temperature. The temperature dependence of the hole concentration for both films

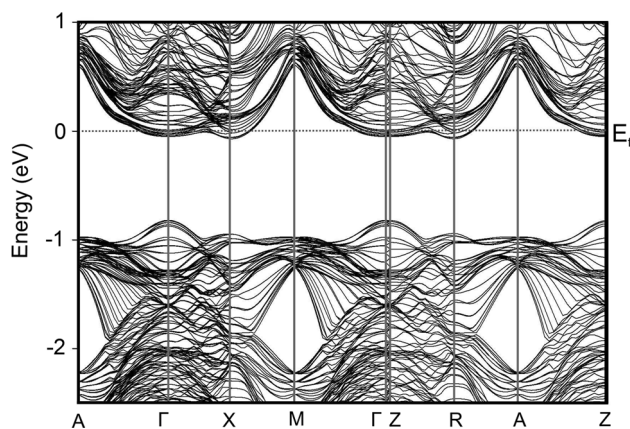
demonstrates a high value of  $\sim 10^{20-21} \text{ cm}^{-3}$ , ( $\sim 4.2 \times 10^{20} \text{ cm}^{-3}$  at  $T = 77$  K for both samples) which increases when the temperature decreases. The carrier concentration exhibits a plateau at low temperatures, which is characteristic of heavily doped semiconductors. Such behaviour is typical for p-type degenerate conduction. For instance, concentrations of  $1.78 \times 10^{21}$  [48],  $1.54$ – $1.81 \times 10^{21} \text{ cm}^{-3}$  [49] have been observed at room temperature.

### Electronic properties

According to valence electron count rule, the appearance of n-type conductivity is expected for the defect-free  $\text{Mn}_{17}\text{Si}_{30}$  compound. However, the Hall effect measurements did show p-type conductivity for both samples. A possible cause of this disagreement was examined via ab initio calculations. First,  $\text{Mn}_4\text{Si}_7$  and  $\text{Mn}_{17}\text{Si}_{30}$  unit cells were fully optimised without any constraints on the lattice constants. During the DFT electronic structure calculations of  $\text{Mn}_{17}\text{Si}_{30}$ , it was found that the magnetic moment ordering on Mn atoms is very unstable and prone to fluctuations arising from peculiarities of electronic minimisation routines. Typically, the directions of magnetic moments were the same within  $xy$  atomic planes, but showed no clear correlations along the  $z$  axis. Typically, about 20 out of 68 Mn atoms in the unit cell had magnetic moments of 0.1–0.3  $\mu_B$  per atom and the rest had no magnetic moment. Subsequent non-spin polarised calculations showed that the energy difference between such a magnetic state

and fully non-magnetic is only 53 meV per unit cell (188 atoms), which hardly has relevant physical meaning. The calculations of the  $\text{Mn}_{17}\text{Si}_{30}$  unit cell with one Si vacancy also revealed no magnetic ordering. Thus, all the results concerning this phase are presented for the non-magnetic case. Then,  $\text{Mn}_{17}\text{Si}_{30}$  compound can be considered as a material with good thermoelectric performance since it will not suffer from spin disorder-induced degradation of the charge [50]. The  $\text{Mn}_4\text{Si}_7$  showed no magnetic behaviour, but the vacancies within its structure possess unpaired electrons with free magnetic moment.

The optimised lattice parameters for  $\text{Mn}_4\text{Si}_7$  ( $a$ ,  $b = 5.498$  and  $c = 17.350$  ) and  $\text{Mn}_{17}\text{Si}_{30}$  ( $a$ ,  $b = 5.505$  and  $c = 73.840$  Å) agree well with known single-crystal experiments. In case of  $\text{Mn}_4\text{Si}_7$  unit cell deviation of theoretically calculated lattice parameters from experimental ones are 0.77 and 0.83% for  $a$ ,  $b$  and  $c$ , respectively [41]. Lattice parameters for known ( $\text{Mn}_{0.8}\text{Cr}_{0.25}$ ) $_{17}\text{Si}_{30}$  compound [24] differ from the determined ones of  $\text{Mn}_{17}\text{Si}_{30}$  on 0.81 and 0.99%, for  $a$ ,  $b$  and  $c$ , respectively. The band structure of  $\text{Mn}_{17}\text{Si}_{30}$  (Fig. 8) indicates its minimum indirect bandgap of 0.745 eV between  $\Gamma$  and X points. The direct transitions have close values (around 0.770 eV) between almost flat band segment along  $\Gamma$  to Z direction. In comparison with a band structure of other higher manganese silicides presented earlier [13, 14], the overall band structure looks similarly, although electron pockets in points R and X of the conduction band are situated lower towards band gap. It has been shown in our experiments that the  $\text{Mn}_{17}\text{Si}_{30}$



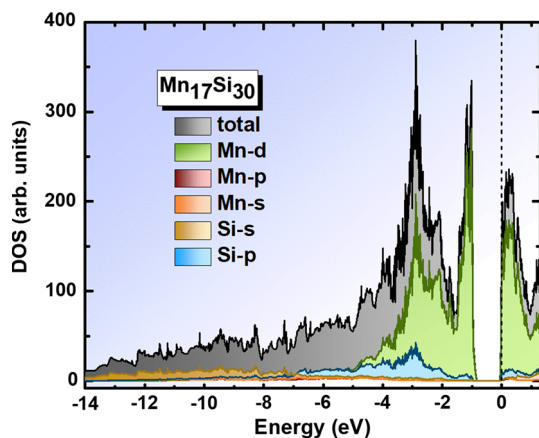
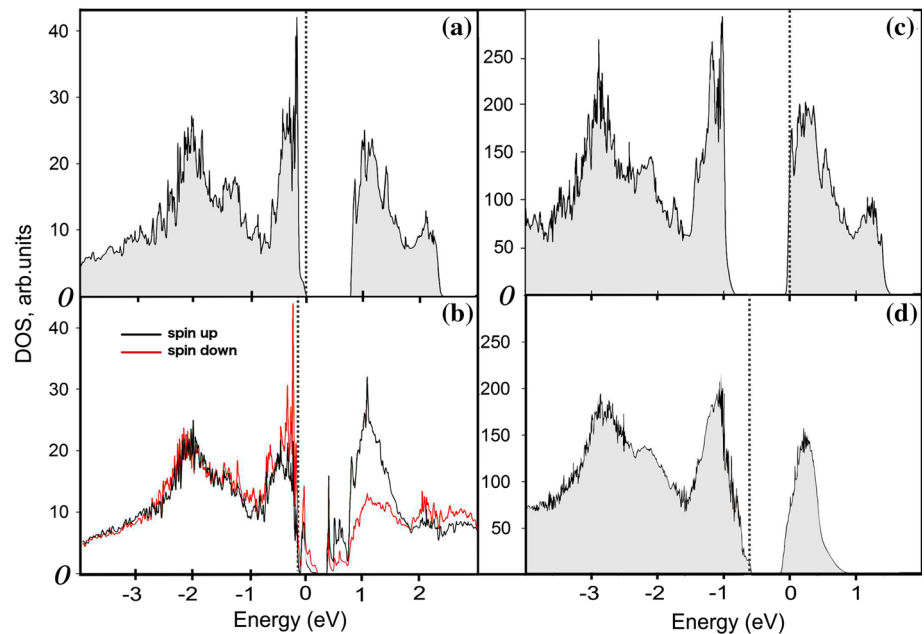
**Figure 8** Band structure of  $\text{Mn}_{17}\text{Si}_{30}$ . Zero at the energy scale corresponds to the Fermi energy.

demonstrates the hole mobility at  $T = 77$  K by one order of magnitude higher than the  $\text{Mn}_4\text{Si}_7$  thin film, 25 and  $2.5 \text{ cm}^2/\text{V s}$ , respectively. Thus, a shift of Fermi level closer to the valence band at invariable conduction band could result in an increase in the hole mobility in comparison with the mobility of electrons due to high curvature of the valence bands (Fig. 8). In turn, the enhanced band valley degeneracy [51] of the  $\text{Mn}_{17}\text{Si}_{30}$  in the conduction band could improve the thermoelectric performance even more.

Ab initio electronic properties assessment of the ideal  $\text{Mn}_4\text{Si}_7$  structure carried out here also corresponds well to the results obtained in [13, 14]. According to our calculations,  $\text{Mn}_4\text{Si}_7$  demonstrates the lowest energy indirect transition from  $\Gamma$  up to Z with the energy of 0.765 eV. Direct transition energy is very close and varies in the range from 0.777 to 0.788 eV between two almost flat bands along  $\Gamma$ –Z line.

Figure 9 shows the energy dependences of total DOSs for  $\text{Mn}_4\text{Si}_7$  and  $\text{Mn}_{17}\text{Si}_{30}$ . Figure 10 shows orbital-projected contribution to the DOS of the  $\text{Mn}_{17}\text{Si}_{30}$  phase. Shape of these dependences is almost the same for both compounds. However, Fermi level position in  $\text{Mn}_4\text{Si}_7$  is characteristic for expected non-degenerate semiconducting nature of that material, with fully occupied valence band and empty conduction band at zero temperature. In contrast, the  $\text{Mn}_{17}\text{Si}_{30}$  compound is a degenerate semiconductor with noticeable concentration of electrons as the charge carriers. This follows the trend observed in other HMS, where the Fermi level lies in the valence band if the  $\text{Si}/\text{Mn} < 1.75$ , and lies at the bottom of the gap if  $\text{Si}/\text{Mn} = 1.75$ . However, predicted sign of the carriers differs from our experimental finding discussed above. Moreover, whereas the band gap value of  $\text{Mn}_4\text{Si}_7$  and  $\text{Mn}_{17}\text{Si}_{30}$  compound is very similar to other HMS phases examined by ab initio methods, the experimental results on bandgap give us the values lying in the range from 0.40 to 0.96 eV for both indirect and direct transitions [5, 13, 52–54]. Different structural defects can cause such a wide range of band gap values observed in HMS compounds. Migas et al. [13] showed earlier that addition of the stacking faults common for  $\text{TiSi}_2$  structures (unit cells are rotated by  $90^\circ$  around the  $z$  axis concerning each other) results in a reduction of the band gap down to 0.31 eV along with expected degenerate nature of the material. One can expect that other crystal structure defects, such as silicon and manganese vacancies, can

**Figure 9** DOS of defect-free **a**  $\text{Mn}_4\text{Si}_7$  and **c**  $\text{Mn}_{17}\text{Si}_{30}$ ; **b**  $\text{Mn}_4\text{Si}_7$  and **d**  $\text{Mn}_{17}\text{Si}_{30}$  with one silicon vacancy per unit cell.



**Figure 10** Total and projected DOS of  $\text{Mn}_{17}\text{Si}_{30}$ .

also alter the HMS band structure. It should be noted that HMS tetragonal compound appeared to have such structural defects as silicon helices shifts, which can unsystematically change along the specimen, giving rise to spatially varying orientation anomalies [15].

The p-type conductivity revealed in our  $\text{Mn}_{17}\text{Si}_{30}$  sample, along with its degeneracy (Fig. 7), points out the presence of silicon vacancies in the  $\text{Mn}_{17}\text{Si}_{30}$  thin film synthesised. It was shown in works of Migas et al. [13] and Carpara et al. [14] that non-stoichiometry caused by intrinsic defects, the absence of silicon atom or the presence of additional silicon atom can result in the transformation of degeneracy into non-degeneracy and vice versa. Thus,  $\text{Mn}_{11}\text{Si}_{19}$

and other p-type HMS degenerated semiconductors become p-type non-degenerate as additional silicon atom is added per their unit cells. As a result, the  $\text{Mn}_{11}\text{Si}_{19}$  stoichiometry becomes equal to 1.75 Si/Mn ratio as in  $\text{Mn}_4\text{Si}_7$  phase. Therefore, one can conclude that degeneracy disappears at this value. In turn, silicon vacancies make  $\text{Mn}_4\text{Si}_7$  to show metallicity. Further silicon reduction in  $\text{Mn}_{11}\text{Si}_{19}$  and other degenerate p-type semiconductors gives rise to the appearance of 100% spin-polarisation. Hence, one can expect that an n-type HMS compound with  $\text{Mn}_{17}\text{Si}_{30}$  crystal structure can transform into p-type degenerated semiconductor if contains enough silicon vacancies. The valence electron rule displays that formation of n-type conductivity appears at VEC value of 14.03, while 14 is the lower limit where HMS-based phases ( $\text{Mn}_4\text{Si}_7$  stoichiometry) are not degenerated semiconductors. The stoichiometry closest to  $\text{Mn}_4\text{Si}_7$  (1.75) HMS compound with space group and atoms' fractional coordinates reported,  $\text{Mn}_{27}\text{Si}_{47}$  (1.741) demonstrates metallic properties, VEC = 13.96. The newly discovered  $\text{Mn}_{17}\text{Si}_{30}$  compound with *I-42d* space group contains 120 silicon and 68 manganese atoms (Si/Mn = 1.765), with VEC equal to 14.06. Thus, one silicon vacancy per  $\text{Mn}_{17}\text{Si}_{30}$  unit cell results in Si/Mn = 1.75, VEC = 14 and withdraws degeneracy. In turn, divacancy should transform  $\text{Mn}_{17}\text{Si}_{30}$  into degenerate semiconductor, Si/Mn = 1.735, VEC = 13.94. While the issue of the silicon vacancy along with introduction of an

additional silicon atom has already been illuminated in the literature, consideration of how Mn vacancies affect electronic properties of HMS phases is poorly examined. A removal of one manganese atom from  $\text{Mn}_4\text{Si}_7$  crystal structure gives  $\text{Si}/\text{Mn} = 1.867$ ,  $\text{VEC} = 14.47$ , for  $\text{Mn}_{17}\text{Si}_{30}$  –  $\text{Si}/\text{Mn} = 1.791$ ,  $\text{VEC} = 14.16$ .

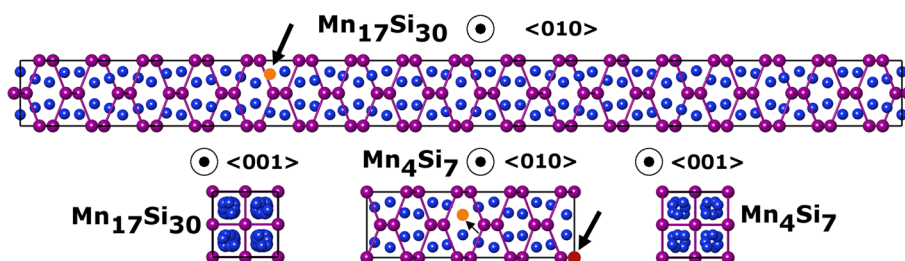
Next, we tried to figure out how the introduction of Mn and Si vacancies affects electronic properties of these HMS phases. In the plane wave basis DFT calculations, low concentration intrinsic defects are usually modelled by an extended supercell. However, in our case, such approach is not practically applicable in view of the large  $\text{Mn}_{17}\text{Si}_{30}$  unit cell. Due to this reason, we had to use a model with one vacancy per unit cell with the hope of obtaining correct qualitative results. Introducing silicon or manganese vacancies, we relaxed the atomic positions in the unit cell without optimisation of lattice parameters. Figure 11 depicts the position of silicon and manganese vacancies in the  $\text{Mn}_4\text{Si}_7$  unit cell. One silicon vacancy is placed in the plane (0 0 2.15) or the 8j Wyckoff position. Manganese vacancy is located in 2c Wyckoff position, (001) plane. In case of the  $\text{Mn}_{17}\text{Si}_{30}$  compound, silicon vacancy is situated in (004) plane, 16e Wyckoff position.

As in the previous theoretical investigation of the silicon vacancy influence on the electronic properties of  $\text{Mn}_4\text{Si}_7$  compound [14] our calculations indicate a transformation of  $\text{Mn}_4\text{Si}_7$  into a degenerate semiconductor. The total DOS corresponding to the  $\text{Mn}_4\text{Si}_7$  with one silicon vacancy is shown in Fig. 9b. One can easily see the appearance of empty states for spin down electrons just above the top of the valence band and below the conduction band. However, the band gap as intrinsic characteristic remains for both spin up and spin down electron states, almost not changing its value. We assume that at finite

temperatures, electrons will be transferred to the empty defect states inside the band gap from the valence band, leaving holes there. Thus, we conclude that introduction of Si vacancies results in p-doping of  $\text{Mn}_4\text{Si}_7$ . While manganese atoms contribute more valence electrons to the structure than silicon (7 against 4), the Mn vacancy gives rise to more drastic changes in the electronic structure of  $\text{Mn}_4\text{Si}_7$ . For both spin down and spin up electrons, new allowed energy states appear in the band gap and the Fermi level is placed inside this new states (see Supplementary Fig. S2). As a result,  $\text{Mn}_4\text{Si}_7$  becomes metallic. Even for four times lower concentration of Mn vacancies (one vacancy per  $2 \times 2 \times 1$  supercell, see Fig. S2b), both empty and filled states are created inside the bandgap, which leads to significant transition energy reduction and no clear doping sign.

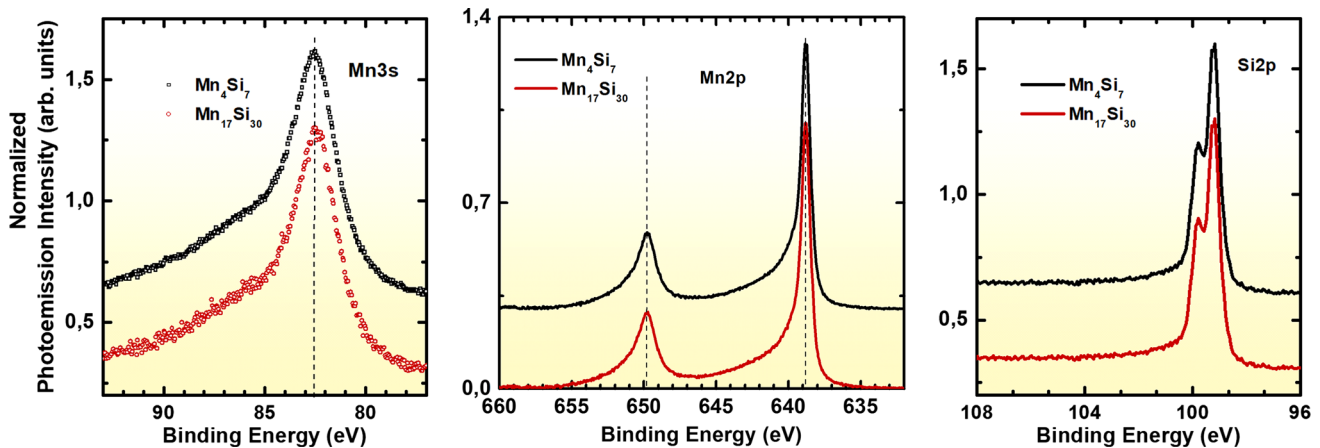
Thus, we assume that p-doping of  $\text{Mn}_{17}\text{Si}_{30}$  observed in the experiment may originate from the high concentration of Si vacancies in the structure. Indeed, new states are introduced above the valence band maximum (4 electron states per unit cell), which pulls all electrons from the conduction band. Extrapolating this effect for slightly higher Si vacancy concentrations, the defective  $\text{Mn}_{17}\text{Si}_{30}$  is expected to be a p-doped semiconductor.

Figures 12 and 13 show the spectra of core levels and valence bands (VB) of  $\text{Mn}_4\text{Si}_7$  and  $\text{Mn}_{17}\text{Si}_{30}$  obtained with X-ray photoelectron spectroscopy. The A, B and C marks (Fig. 13) indicate spectral regions of interest for the valence electrons of particular orbital symmetry. The VB spectra slightly differ from each other. The reason for this, in part, is that the compounds under consideration are homologous phases with a similar crystal structure and differ in the concentration of the elements by less than 1%. The same applies to the core level spectra of Mn and Si. The Mn 2p core level spectra of the  $\text{Mn}_4\text{Si}_7$  and

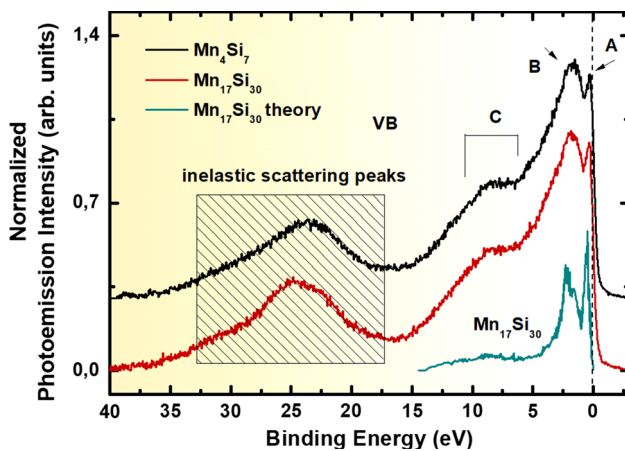


**Figure 11** Crystal structure of  $\text{Mn}_4\text{Si}_7$  and  $\text{Mn}_{17}\text{Si}_{30}$  (view along [010] and [001]). Purple and blue circles are the Mn and Si atoms, respectively; Silicon and manganese vacancies introduced for

calculation of defects are depicted by an orange circle and a red circle with arrows in  $\text{Mn}_4\text{Si}_7$ , respectively.  $\text{Mn}_{17}\text{Si}_{30}$  unit cell contains only silicon vacancy.



**Figure 12** Mn 3s left panel, Mn 2p central panel and Si 2p right panel core level spectra of  $\text{Mn}_4\text{Si}_7$  and  $\text{Mn}_{17}\text{Si}_{30}$  thin films.



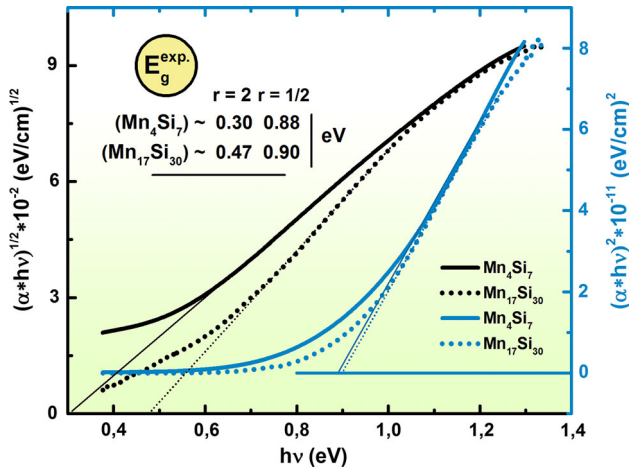
**Figure 13** Valence band spectra of  $\text{Mn}_4\text{Si}_7$  and  $\text{Mn}_{17}\text{Si}_{30}$  thin films. The blue line shows the calculated total DOS. These calculated valence band spectra result from the summation of the densities of states of electrons of various orbital symmetries with allowance for their photoionisation cross sections for  $E_{\text{ex}} = 1486$  eV and the atomic concentration. Peaks A–C correspond to different states in the VB spectra. The shaded region of the valence band at a binding energy of 17–33 eV is formed by plasmon satellites. The energy scale refers to the valence band maximum.

$\text{Mn}_{17}\text{Si}_{30}$  films (Fig. 12) do not differ in their form and energy value from Mn 2p spectra of  $\text{La}_{1-x}\text{Sm}_x\text{Mn}_2\text{Si}_2$  disilicides and pure Mn [55]. The multiplet energy splitting of the Si 2p level is well resolved; there are no satellites in the spectra, which can be associated with oxidation of the samples (Figs. 12 and S3). The valence band spectra for both compounds are additive and reflect the sum of contributions from the Si 3p, 3s, and Mn 3d electronic states in the energy range 0–15 eV. According to the theoretical calculations (Fig. 10), Mn 3d states occupy the region  $\Delta E \approx 5$  eV at the top of occupied valence zone. A

narrow Mn 3d subband A is observed below the Fermi energy in the spectrum, the position and shape of which is in good agreement with the results of the calculations. The Si 3p (band B) and Si 3s (band C) states occupy an interval with binding energy from 8 to 14 eV, which have been experimentally observed in some works [56]. The concentration of silicon atoms is more than 1.75 times higher than the concentration of manganese atoms, the atomic subshell photoionisation cross sections at an excitation energy of 1486 eV are equal to  $\sigma_{\text{Si}3s} = 0.1 \times 10^{-2}$ ,  $\sigma_{\text{Si}3p} = 0.17 \times 10^{-3}$  и  $\sigma_{\text{Mn}3d} = 0.14 \times 10^{-2}$  [57].

Total DOS was plotted taking into account the atomic subshell photoionisation cross sections and the component concentration of the  $\text{Mn}_{17}\text{Si}_{30}$  compound. We note that the shape and energy position of the subbands in DOS are in good agreement with the experimental spectrum. In our photoemission study, a presence of an energy gap in the vicinity of the Fermi energy is not observed, which is consistent with the examination of transport characteristics. The presence of a dielectric gap in a sample at X-ray irradiation leads to charging of the sample under study, which depends on the size of the gap. However, there could be defects (silicon vacancies) in the films we studied, which lead to partial degradation of the gap, due to the lowering of the atomic symmetry of the local environment and the appearance of discrete energy levels in the gap. X-ray favours the generation of an avalanche of electrons in the continuum of the crystal due to the Auger decay of excited atoms, the migration of holes (in the electron shells of atoms) to the top of the filled band and the charge flow. A typical example is the degradation of





**Figure 14** Tauc plots of  $(\alpha \times hv)^{1/2}$  and  $(\alpha \times hv)^2$  versus  $hv$  for  $Mn_4Si_7$  and  $Mn_{17}Si_{30}$  films = measured at 300 K;  $\alpha$  is the absorption coefficient, and  $hv$  is the photon energy.

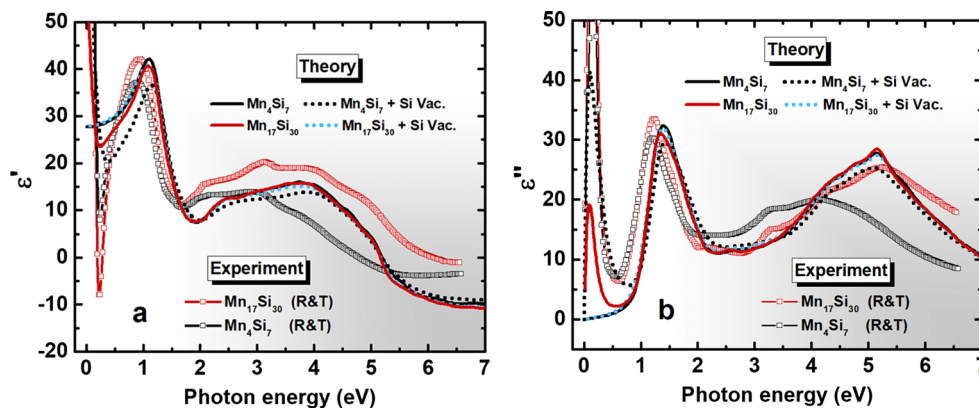
the spin gap in half-metallic magnets, which is observed in Heusler alloys due to a small degree of disordering. Of particular interest is the shaded region of the valence band at a binding energy of 16–35 eV (Fig. 13). This spectrum part is formed by plasmon satellites. According to modern concepts, these plasmons represent a wide spectrum of quasi-particles, which arises as a result of quasifree electron excitation by X-ray photons. The spectrum of quasi-particles in the valence band was first observed in the study of doped single-crystal graphene films [58] and theoretically grounded in [59]. It was also experimentally observed in monocrystalline silicon [60]. This important feature of the spectrum is first observed for the Mn–Si film presented in our work.

We note here that usually the experimental observation of plasmons in the valence band is possible only in high-purity materials not chemically contaminated by oxygen since the 2s ( $E_B = 23$  eV) oxygen spectrum lies in the same energy interval as the plasmon satellite.

The spin–orbit splitting of the Mn 2p spectra in Fig. 12 (central panel) is estimated to be 11 eV. A complex multiplet structure is absent below the main parts of the spin–orbit splitting. For  $Mn_4Si_7$  the sharp peak A ranging from  $-0.3$  eV to the Fermi level ( $E_F$ ) and for  $Mn_{17}Si_{30}$   $-0.4$  eV to the Fermi level, respectively, have dominantly a Mn-3d character, consistent with the experimentally observed p-type semiconducting behaviour. Such a steep DOS near  $E_F$  is a prerequisite for realising a good p-type thermoelectric material because Seebeck coefficient is proportional to the energy derivative of DOS at  $E_F$ . A broad peak B at  $E = -3$  to  $-1$  eV can be characterised by the Mn-3d and Si-2p bonding states.

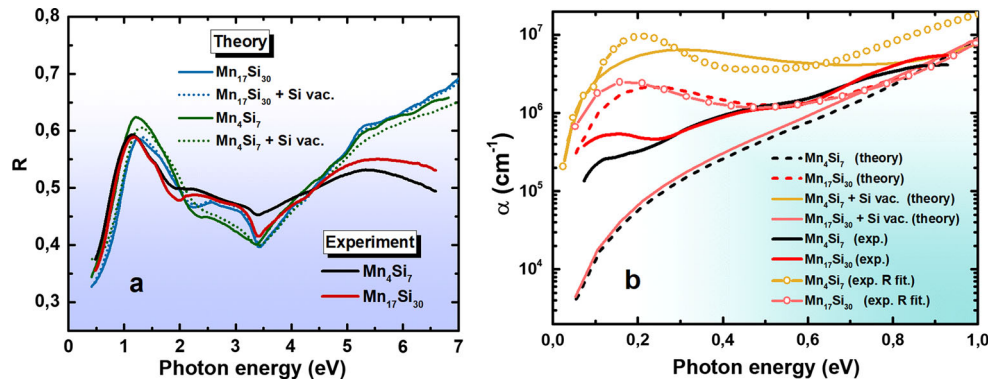
### Optical properties

It has been shown above that electronic structure of  $Mn_4Si_7$  and  $Mn_{17}Si_{30}$  is very sensitive to intrinsic defects (silicon or manganese vacancies). Mainly, the vacancy introduction appears to affect the bandgap region and the Fermi level displacement while the ground states remain almost unchanged. Thus, such defects can influence the optical characteristics so that the visible photon energy range will be almost the same for all HMS phases with or without vacancy due to the fact that the formation of the permittivity



**Figure 15** Real (a) and imaginary (b) parts of permittivity spectra obtained by ab initio calculations for the ideal (black solid— $Mn_4Si_7$ , red— $Mn_{17}Si_{30}$ ) and defected (dotted black— $Mn_4Si_7$ , blue— $Mn_{17}Si_{30}$ ) unit cells and the spectra determined by the Drude–

Lorentz model for the  $Mn_4Si_7$  and  $Mn_{17}Si_{30}$  samples through processing of experimental reflectance and transmittance spectra (black squares— $Mn_4Si_7$ , red squares— $Mn_{17}Si_{30}$ ).



**Figure 16** Reflectance spectra of **a**  $\text{Mn}_4\text{Si}_7/\text{Si}(001)$  (solid black line) and  $\text{Mn}_{17}\text{Si}_{30}/\text{Si}(001)$  (solid red line) measured at near-normal incidence. Green and blue lines correspond to the reflectance spectra obtained for HMS/Si(001) system using ab initio calculated  $\text{Mn}_4\text{Si}_7$  and  $\text{Mn}_{17}\text{Si}_{30}$  permittivity. Solid and dotted lines depict the ideal structures and with silicon vacancies,

spectra is caused by electron transitions from the valence to conductive band. Conversely, low-energy spectra region should reflect such changes, which electronic structure of HMS compounds undergoes. Such changes are the Fermi level movement to and from the valence band and the formation of allowed energy states inside the band gap. Below we consider optical characteristic (reflectance, permittivity and coefficient of absorption) obtained within both experimental and theoretical approaches.

Figure 14 presents Tauc plot of  $(\alpha \times hv)^{1/r}$  for allowed direct ( $r = 1/2$ ) and indirect ( $r = 2$ ) transitions for both samples ( $\text{Mn}_4\text{Si}_7$  and  $\text{Mn}_{17}\text{Si}_{30}$ ). Therefore, evaluating linear regions on the Tauc plot curves for both samples we conclude that both samples have a direct bandgap with slightly different transition energies of  $\sim 0.88$  and  $0.9$  eV for  $\text{Mn}_4\text{Si}_7$  and  $\text{Mn}_{17}\text{Si}_{30}$ , respectively, which is in good agreement with the experimental data on HMS films bandgap values [53]. Below the lowest direct transition, indirect gaps of  $0.3$  ( $\text{Mn}_4\text{Si}_7$ ) and  $0.47$  ( $\text{Mn}_{17}\text{Si}_{30}$ ) eV are observed. H. Lange obtained indirect transition with a value of  $0.46$  eV taking into account phonon absorption and emission [5]. The value given in our work is calculated excluding phonon impact. As it will be shown below, the low-energy part is strongly influenced by low-energy electron transitions caused by the degeneracy of  $\text{Mn}_4\text{Si}_7$  and  $\text{Mn}_{17}\text{Si}_{30}$  samples (Fig. 15b). Band structures for both  $\text{Mn}_4\text{Si}_7$  and  $\text{Mn}_{17}\text{Si}_{30}$  phases indicate that indirect and direct transitions are very close to each other with the value around  $0.8$  eV. Thus, indirect transition observed by

respectively, **b** experimental coefficient of absorption in low photon energy region ( $0.07$ – $1$  eV).  $\alpha$  spectra calculated using the permittivity obtained by KK-constrained analysis are presented along with ab initio calculated for ideal and defected  $\text{Mn}_4\text{Si}_7$  and  $\text{Mn}_{17}\text{Si}_{30}$  unit cells.

many authors [5, 13, 53] is possibly caused by defect structure. Specifically, Migas et al. [13] showed that a possible reason for reducing bandgap could be a presence of stacking faults [13]. Our XRD study shows no clear evidence for existence of stacking faults in our samples. Alternatively, the coexistence of indirect ( $\sim 0.4$ ) and direct transitions can be explained by influence of high concentration of vacancies that can considerably modify band structure [14], additionally producing asymmetry of transitions for electrons with opposite spin orientation.

According to the band structures of ideal  $\text{Mn}_{17}\text{Si}_{30}$  and  $\text{Mn}_4\text{Si}_7$  calculated in this work, direct transition energies are around  $0.78$  eV, which is 11% less than experimental values. In addition to the absorption edge examination of the polycrystalline  $\text{Mn}_4\text{Si}_7$  and  $\text{Mn}_{17}\text{Si}_{30}$  films, we also attempted to display peculiarities in spectra of their reflectance, and real and imaginary part of permittivity in the range  $0.18$ – $17$   $\mu\text{m}$  by means of modelling the reflectance and transmittance spectra. The permittivity spectra over the whole range mentioned were obtained by modelling a combination of reflectance and transmittance spectra with the help of Reffit software [61] by Kramers–Kronig (KK) constrained variational analysis [62].

Figure 16a shows the experimental reflectance spectra for both samples. The spectra obtained exhibit similar behaviour at photon energies below  $2$  eV, diverging noticeably above  $2$  eV. Minor difference caused by the slightly higher band gap of  $\text{Mn}_{17}\text{Si}_{30}$  is

also observable in the near-infrared region, below 1 eV. Visible region of the spectra seems to be sensitive to the relative film thickness spread. The more pronounced decrease in the reflectance at the photon energies around 2 and 3.5 eV for  $\text{Mn}_{17}\text{Si}_{30}$  is due to a smaller relative thickness spread of the film, which is 0.26 according to the fitting procedure carried out with use of ab initio calculated spectra. This value is in a good accordance with the experimental value of 0.3 obtained by TEM methods. The  $\text{Mn}_{17}\text{Si}_{30}$  film thickness obtained (17.8 nm) also agrees well with the TEM results. The relative thickness spread (0.521) and the film thickness (27.2 nm) in case of the  $\text{Mn}_4\text{Si}_7$  sample determined by the fitting procedure do not contradict the TEM data. Thus, one can conclude that the  $\text{Mn}_4\text{Si}_7$  and  $\text{Mn}_{17}\text{Si}_{30}$  permittivity spectra obtained from ab initio calculations are in good agreement with experiment over the visible and near-infrared regions, even though the bandgap values were estimated not precisely. Besides, the experimental reflectance spectra diverge largely in the ultraviolet region with ab initio constrained ones. Nevertheless, the higher UV reflectance of  $\text{Mn}_{17}\text{Si}_{30}$  in comparison with the  $\text{Mn}_4\text{Si}_7$  case for ab initio calculations is also observed in experimental spectra (Fig. 16a). We examined possible influence of  $\text{SiO}_2$  native oxide layer above the film, according to [53], to the results of modelling, too. Assuming that thickness of this layer was of order of several nm (Fig. 5), we have found that it must not significantly change the behaviour of the reflectance spectra. Therefore, further, we excluded it from the consideration.

It is expected that the degeneracy of the higher manganese silicides should strongly affect the behaviour of absorption coefficient below 0.5 eV. The absorption coefficient should demonstrate an increase when the Fermi level goes into the valence band so that the low-energy transitions can take place from the electron states beneath the Fermi level to the unoccupied states closely above Fermi level. First, we look at the IR spectra (Fig. 16b) recalculated from net experimental data by subtracting the absorbance of a clean Si(001) substrate from the absorbance of HMS/Si(001) (solid black and red curves for  $\text{Mn}_4\text{Si}_7$  and  $\text{Mn}_{17}\text{Si}_{30}$ , respectively) and then normalising them to the film thickness. One can easily see that coefficient of absorption of  $\text{Mn}_{17}\text{Si}_{30}$  thin film is much higher than in case of the  $\text{Mn}_4\text{Si}_7$  sample, thus indicating its degenerate nature. The spectra corresponded to ab initio calculations for ideal  $\text{Mn}_4\text{Si}_7$  and  $\text{Mn}_{17}\text{Si}_{30}$

unit cells (dash black and red curves for  $\text{Mn}_4\text{Si}_7$  and  $\text{Mn}_{17}\text{Si}_{30}$ , respectively) show similar behaviour. However, the experimental peak centred near 0.15 eV has narrower width than the theoretical one. As it was shown earlier, the calculated Fermi level for vacancy-free  $\text{Mn}_{17}\text{Si}_{30}$  compound is located inside the conductance band near its bottom, resulting in the expected prominent peak on the coefficient of absorption spectra around 0.2 eV. However, similar peak must be expected for the case when Fermi level crosses upper sublevels of the valence band. Conversely, the experimental  $\text{Mn}_{17}\text{Si}_{30}$  sample demonstrates p-type conductivity that along with its metallic behaviour (Fig. 7) and behaviour of the coefficient of absorption indicates that Fermi level is inside the valence band. Thus, the  $\text{Mn}_{17}\text{Si}_{30}$  film should contain a significant quantity of silicon vacancies, namely more than one vacancy per  $\text{Mn}_{17}\text{Si}_{30}$  unit cell for shifting the Fermi level down to the valence band. A closer look at the black solid curve (Fig. 16b— $\text{Mn}_4\text{Si}_7$  exp.) makes it clear that  $\text{Mn}_4\text{Si}_7$  is also a degenerate semiconductor. The theoretical curve (dash black) does not reveal any increase in the coefficient of absorption around 0.15 eV, whereas the experimental one (solid black) does. Further, introducing one silicon vacancy into  $\text{Mn}_4\text{Si}_7$  unit cell gives rise to a significant increment of the coefficient of absorption (yellow solid) over the whole region plotted. Hence, we conclude that the  $\text{Mn}_4\text{Si}_7$  thin film contains silicon vacancies as high as one vacancy per unit cell and less than the  $\text{Mn}_{17}\text{Si}_{30}$  sample.

Additionally, we plotted the coefficient of absorption spectra obtained by converting the permittivity spectra (Fig. 15) determined with the KK-constrained fitting of reflectance (0.5–6.63 eV) and transmittance (0.07–1 eV) spectra combination. The fitting procedure used an adjustment of three harmonic oscillator parameters within the Drude–Lorentz model at fixed thickness values without consideration of Fabry–Perot effect, which we suppose is suppressed due to the significant roughness of the silicon substrate rear side. As a result, the coefficient of absorption peak around 0.2 eV (solid yellow curve with circles) for the  $\text{Mn}_4\text{Si}_7$  sample became more significant and the curve corresponding to the  $\text{Mn}_{17}\text{Si}_{30}$ —closer to the theoretical one for ideal  $\text{Mn}_{17}\text{Si}_{30}$ . The coefficient of absorption for  $\text{Mn}_{17}\text{Si}_{30}$  unit cell containing the silicon vacancy (solid pink curve) has the same behaviour as in case of defect-free  $\text{Mn}_4\text{Si}_7$  unit cell. Therefore, a further increment of silicon vacancies

per  $\text{Mn}_{17}\text{Si}_{30}$  unit cell will result in the same behaviour as in case of the  $\text{Mn}_4\text{Si}_7$  unit with one silicon vacancy.

Real and imaginary part of the permittivity for the ideal and defected  $\text{Mn}_4\text{Si}_7$  and  $\text{Mn}_{17}\text{Si}_{30}$  unit cells are presented in Fig. 15. Whereas over the whole photon energy range from the absorption edge the permittivity is almost not influenced by the introduction of silicon vacancies into the unit cell, slight value decrease can be noticed for  $\text{Mn}_4\text{Si}_7$  unit cell with the silicon vacancy (black dotted curve Fig. 15). The only region, which is highly sensitive to the silicon vacancies, is the infrared part of the spectra from 0.05 up to 0.6 eV. The prominent peaks appear due to the degeneracy of  $\text{Mn}_4\text{Si}_7$  and  $\text{Mn}_{17}\text{Si}_{30}$  caused by off-stoichiometry.

The experimental spectra of the permittivity (Fig. 15) obtained through the simultaneous processing of transmittance and reflectance spectra differ noticeably for  $\text{Mn}_4\text{Si}_7$  and  $\text{Mn}_{17}\text{Si}_{30}$ . In case of  $\text{Mn}_{17}\text{Si}_{30}$ , the real part of dielectric constant reaches higher values than in case of the  $\text{Mn}_4\text{Si}_7$  sample, as well as than theoretical curves almost over the whole photon energy region, even though preserving qualitatively the behaviour predicted by theoretical calculations. In turn,  $\epsilon'$  for the  $\text{Mn}_4\text{Si}_7$  undergoes significant changes in comparison with  $\text{Mn}_{17}\text{Si}_{30}$  and with theory for both defected and defect-free  $\text{Mn}_4\text{Si}_7$ . One can notice that a formation wide prominent peak of absorption in imaginary part  $\epsilon''$  around 5 eV is mainly caused by high energy Si 2*p* electron transitions from the ground of the valence band (Fig. 10). This peak shifts towards the lower energy and simultaneously decreases its amplitude in comparison with theoretical curves and the experimental one for  $\text{Mn}_{17}\text{Si}_{30}$ . Such behaviour can be explained by the appearance of allowed states in the bandgap resulted from silicon vacancies (Fig. 9b), which promote the peak shift and its broadening along with an increase in the absorption in intermediate photon energy region from 2 up to 3 eV.

Nevertheless, such behaviour is not described by the introduction of one silicon vacancy per  $\text{Mn}_4\text{Si}_7$  unit cell as the theory shows (Fig. 15 black dotted curve). The transport characteristics of the  $\text{Mn}_4\text{Si}_7$  sample do not demonstrate strong metallicity, which is expected in case of the silicon divacancy in the  $\text{Mn}_4\text{Si}_7$  unit cell. One can look for a possible reason for that in higher intergranular border density (Fig. 6) and in existence of dangling bonds in the  $\text{Mn}_4\text{Si}_7$  film.

Moreover, along with the crystal structure defects typical for HMS compounds, constituting atom vacancy [14], impurities and stacking faults [13] a structural anomaly such as the silicon helices shifts are also reported. It is asserted that silicon atom rows may be shifted along the *c* axis by 0.02 nm w.r.t. adjacent rows of manganese subcell or stepwise every *n*th row of manganese unit cell. According to the work [15] such shift can appear unsystematically along the sample. Every small shift of the silicon helices can create unique surrounding of the manganese atoms, which are responsible for the formation of the top of the valence band and the bottom of the conduction band. One can expect a sophisticated magnetic order or significant changes in optical characteristics. However, examination of how such lattice defect could affect the HMS electronic structure with the help of the ab initio analysis is not possible due to the system size limitations.

The absorption peak at 5.5 eV discussed in case of the  $\text{Mn}_{17}\text{Si}_{30}$  sample shows slight changes on the background of the theory. Moreover, it follows the theoretical curve behaviour for  $\text{Mn}_4\text{Si}_7$  unit cell with one silicon vacancy indicating the existence of two silicon vacancies in  $\text{Mn}_{17}\text{Si}_{30}$  unit cell. The narrow, intense peak at 1.25 eV related to the electron transition from the Mn 3*d* orbitals remains steady and is in good correspondence with ab initio calculation. Hence, we expect that Mn “chimneys” have a perfect quality. The discrepancy in the position of the absorption edge between theoretical and experimental curves can be caused by the underestimation of the bandgap in the DFT method. The amplitude and width of the peak at 0.2 eV are larger than in case of n-type degenerated  $\text{Mn}_{17}\text{Si}_{30}$  compound. This indicates close stoichiometry of the samples obtained despite their different crystal structures.

## Conclusion

Summing up, an approach to alter the phase formation sequence and structural type of higher manganese thin films on silicon substrate during the solid-state reaction was proposed. The approach relies on the effective heat of formation model where, depending on the architecture of initial layer stack comprising pure manganese layer, Mn–Si alloy layers with combination of constant and gradient chemical composition, the two main solid-state reaction fronts

result in a different phase formation sequence at increased temperature. According to the approach proposed, the scheme of starting layer stack was developed for production of new HMS material,  $\text{Mn}_{17}\text{Si}_{30}$ . Polycrystalline  $\text{Mn}_4\text{Si}_7$  and  $\text{Mn}_{17}\text{Si}_{30}$  thin films were grown on silicon substrates Si(001) using the predicted stack structure. The films obtained were characterised to reveal their structural, optical, electronic, transport properties. Morphological details were extracted by TEM and XRD. Results of modelling reflectance and transmittance spectra are in good accordance with experiment and infer that the  $\text{Mn}_4\text{Si}_7$  and  $\text{Mn}_{17}\text{Si}_{30}$  have a thickness of 24 and 18 nm with relative thickness spread of 0.56 and 0.27, respectively. They also demonstrate different size and form of crystallites. While the crystallites of  $\text{Mn}_{17}\text{Si}_{30}$  have high aspect ratio more than 4, the  $\text{Mn}_4\text{Si}_7$  crystallites are less in size and demonstrate in average low aspect ratio. The difference in physical properties is caused by non-equal initial layer stack.

The electronic structure and optical properties of  $\text{Mn}_4\text{Si}_7$  and  $\text{Mn}_{17}\text{Si}_{30}$  compound were examined using ab initio calculations. While  $\text{Mn}_4\text{Si}_7$  phase and all other well-known HMS compounds are p-type semiconductors, density functional theory calculations showed that the Fermi level in ideal  $\text{Mn}_{17}\text{Si}_{30}$  electronic structure lies inside the conductivity band that identifies it as an n-type degenerate semiconductor. It is concluded that  $\text{Mn}_{17}\text{Si}_{30}$  and  $\text{Mn}_4\text{Si}_7$  can be either degenerate or non-degenerate by introducing one silicon vacancy per unit cell. The Hall measurements in this work indicate that  $\text{Mn}_{17}\text{Si}_{30}$  is a p-type degenerate semiconductor with the Hall mobility as high as  $25 \text{ cm}^2/\text{Vs}$  at  $T = 77 \text{ K}$ . Optical absorbance experimental spectra in low photon energy region below the optical absorbance edge show a prominent peak for  $\text{Mn}_4\text{Si}_7$  and  $\text{Mn}_{17}\text{Si}_{30}$  thin films obtained. The behaviour of the imaginary part of the permittivity is an evidence for the films containing silicon vacancies in their crystal structures.

Besides, experimental study of the optical properties in wide photon energy range (0.076–6.55 eV) reveals their sensitivity to intrinsic defects. We observed a noticeable difference in the dielectric function spectra of the  $\text{Mn}_{17}\text{Si}_{30}$  and  $\text{Mn}_4\text{Si}_7$  films assuming that Si 2p electron ground states of the  $\text{Mn}_4\text{Si}_7$  sample are deformed. Further investigation of controllable synthesis of different higher manganese silicide thin film on a silicon substrate and controllable defect formation is needed. Such methods as

electronic paramagnetic resonance and Raman spectroscopy could be fruitful for examination of the defect formation in higher manganese silicides. We believe a deeper insight into the controllable formation of defects in higher manganese silicide thin films on silicon and other substrates could open wide opportunities for their application in thermoelectrics, photovoltaics and optoelectronics.

## Acknowledgements

This work was supported by the Russian Science Foundation, Project No. 16-13-00060. Aleksandr S. Aleksandrovsky thanks RFBR Grant No. 17-52-53031 for partial work related to the NIR measurements in section “Optical Properties”. The authors are grateful to Dr. A.V. Mudriy of Minsk State University for technical assistance. The equipment of the Center for Shared Use of Federal Research Center KSC SB RAS and the Ural Center “Modern Nanotechnology” of Ural Federal University was used.

**Electronic supplementary material:** The online version of this article (<https://doi.org/10.1007/s10853-018-2105-y>) contains supplementary material, which is available to authorized users.

## References

- [1] Barczak SA, Downie RA, Popuri SR et al (2015) Thermoelectric properties of Fe and Al double substituted  $\text{MnSi}_y$  ( $y \sim 1.73$ ). *J Solid State Chem* 227:55–59. <https://doi.org/10.1016/j.jssc.2015.03.017>
- [2] Tada S, Isoda Y, Udono H et al (2013) Thermoelectric properties of p-type  $\text{Mg}_2\text{Si}_{0.25}\text{Sn}_{0.75}$  doped with sodium acetate and metallic sodium. *J Electron Mater* 43:1–5. <https://doi.org/10.1007/s11664-013-2797-3>
- [3] Chen X, Weathers A, Carrete J et al (2015) Twisting phonons in complex crystals with quasi-one-dimensional substructures. *Nat Commun* 6:6723. <https://doi.org/10.1038/ncomms7723>
- [4] Bogala MR, Reddy RG (2017) Reaction kinetic studies of metal-doped magnesium silicides. *J Mater Sci* 52:11962–11976. <https://doi.org/10.1007/s10853-017-1095-5>
- [5] Mahan JE (2004) The potential of higher manganese silicide as an optoelectronic thin film material. *Thin Solid Films* 461:152–159. <https://doi.org/10.1016/j.tsf.2004.02.090>

- [6] III/17G-41D CA, Editors of the volumes (2000)  $Mn_{(n)}Si_{(2n-m)}$ : space group, lattice parameters of  $Mn_{(n)}Si_{(m-n)}$  and  $(Mn_{(1-x)}T_{(x)})_nSi_{(2n-m)}$  systems. In: Madelung O, Rössler U, Schulz M (eds) Non-tetrahedrally bonded elements and binary compound II. Springer, Berlin, pp 1–2
- [7] Kawasumi I, Sakata M, Nishida I, Masumoto K (1981) Crystal growth of manganese silicide,  $MnSi_{\square 1.73}$  and semiconducting properties of  $Mn_{15}Si_{26}$ . *J Mater Sci* 16:355–366. <https://doi.org/10.1007/BF00738624>
- [8] Mogilatenko A, Falke M, Teichert S et al (2002) Surfactant mediated growth of  $MnSi_{1.7}$  layers on (001)Si. *Microelectron Eng* 64:211–218. [https://doi.org/10.1016/S0167-9317\(02\)00789-X](https://doi.org/10.1016/S0167-9317(02)00789-X)
- [9] Mogilatenko A, Falke M, Hortenbach H et al (2006) Surfactant effect of Sb on the growth of  $MnSi_{1.7}$  layers on Si(0 0 1). *Appl Surf Sci* 253:561–565. <https://doi.org/10.1016/j.apsusc.2005.12.117>
- [10] Higgins JM, Schmitt AL, Guzei IA, Jin S (2008) Higher manganese silicide nanowires of nowotny chimney ladder phase. *J Am Chem Soc* 130:16086–16094. <https://doi.org/10.1021/ja8065122>
- [11] Liu H, She G, Ling S et al (2011) Ferromagnetic Si/ $Mn_{27}Si_{47}$  core/shell nanowire arrays. *J Appl Phys* 109:4–8. <https://doi.org/10.1063/1.3548939>
- [12] Pokhrel A, Degregorio ZP, Higgins JM et al (2013) Vapor phase conversion synthesis of higher manganese silicide ( $MnSi_{1.75}$ ) nanowire arrays for thermoelectric applications. *Chem Mater* 25:632–638. <https://doi.org/10.1021/cm3040032>
- [13] Migas D, Shaposhnikov V, Filonov A et al (2008) Ab initio study of the band structures of different phases of higher manganese silicides. *Phys Rev B* 77:1–9. <https://doi.org/10.1103/PhysRevB.77.075205>
- [14] Caprara S, Kulatov E, Tugushev VV (2012) Half-metallic spin polarized electron states in the chimney-ladder higher manganese silicides  $MnSi_{1-x}$  ( $x = 1.75 - 1.73$ ) with silicon vacancies. *Eur Phys J B* 85:149. <https://doi.org/10.1140/epjb/e2012-30034-2>
- [15] Ye HQ, Amelinckx S (1986) High-resolution electron microscopic study of manganese silicides  $MnSi_{2-x}$ . *J Solid State Chem* 61:8–39. [https://doi.org/10.1016/0022-4596\(86\)90003-4](https://doi.org/10.1016/0022-4596(86)90003-4)
- [16] De Ridder R, Amelinckx S (1971) The structure of defect manganese silicides. *Mater Res Bull* 6:1223–1234. [https://doi.org/10.1016/0025-5408\(71\)90058-4](https://doi.org/10.1016/0025-5408(71)90058-4)
- [17] Miyazaki Y, Saito Y, Hayashi K et al (2011) Preparation and thermoelectric properties of a chimney-ladder ( $Mn_{1-x}Fe_x$ )Si  $\gamma$  ( $\gamma \square 1.7$ ) solid solution. *Jpn J Appl Phys* 50:35804. <https://doi.org/10.1143/JJAP.50.035804>
- [18] Allam A, Boulet P, Record MC (2014) Substitutional atom influence on the electronic and transport properties of  $Mn_4Si_7$ . *J Electron Mater* 43:761–773. <https://doi.org/10.1007/s11664-013-2936-x>
- [19] Allam A, Boulet P, Record M-C (2014) DFT calculations of electronic and transport properties of substituted  $Mn_4Si_7$ . *J Alloys Compd* 584:279–288. <https://doi.org/10.1016/j.jallcom.2013.09.069>
- [20] Hou QR, Gu BF, Chen YB et al (2014) Layer-by-layer deposition of  $MnSi_{1.7}$  film with high Seebeck coefficient and low electrical resistivity. *Mater Chem Phys* 146:346–353. <https://doi.org/10.1016/j.matchemphys.2014.03.035>
- [21] Hou QR, Zhao W, Chen YB, He YJ (2010) Preparation of n-type nano-scale  $MnSi_{1.7}$  films by addition of iron. *Mater Chem Phys* 121:103–108. <https://doi.org/10.1016/j.matchemphys.2010.01.016>
- [22] Hou QR, Gu BF, Chen YB (2014) Cu-induced Seebeck peak in HMS/Si film. *Mod Phys Lett B* 28:1450176. <https://doi.org/10.1142/S0217984914501760>
- [23] Hou QR, Zhao W, Chen YB, He YJ (2009) Preparation of n-type higher manganese silicide films by magnetron sputtering. *Int J Mod Phys B* 23:3331–3348. <https://doi.org/10.1142/S0217979209052881>
- [24] Fliether G, Völlenkle H, Nowotny H (1968) Neue Abkömmlinge der  $TiSi_2$ -Struktur. *Monatshefte für Chemie* 99:2408–2415. <https://doi.org/10.1007/BF01154358>
- [25] Kresse G, Furthmüller J (1996) Efficient iterative schemes for ab initio total-energy calculations using a plane-wave basis set. *Phys Rev B* 54:11169–11186. <https://doi.org/10.1103/PhysRevB.54.11169>
- [26] Kresse G, Hafner J (1993) Ab initio molecular dynamics for liquid metals. *Phys Rev B* 47:558–561. <https://doi.org/10.1103/PhysRevB.47.558>
- [27] Blöchl PE (1994) Projector augmented-wave method. *Phys Rev B* 50:17953–17979. <https://doi.org/10.1103/PhysRevB.50.17953>
- [28] Perdew JP, Burke K, Ernzerhof M (1996) Generalized gradient approximation made simple. *Phys Rev Lett* 77:3865–3868. <https://doi.org/10.1103/PhysRevLett.77.3865>
- [29] Gajdoš M, Hummer K, Kresse G et al (2006) Linear optical properties in the projector-augmented wave methodology. *Phys Rev B* 73:45112. <https://doi.org/10.1103/PhysRevB.73.045112>
- [30] Tarasov IA, Visotin MA, Aleksandrovsky AS et al (2017) Si/Fe flux ratio influence on growth and physical properties of polycrystalline  $\beta$ - $FeSi_2$  thin films on Si(100) surface. *J Magn Magn Mater* 440:144–152. <https://doi.org/10.1016/j.jmmm.2016.12.084>
- [31] Tarasov AS, Lukyanenko AV, Tarasov IA et al (2017) Approach to form planar structures based on epitaxial  $Fe_1$

- $-x\text{Si}_x$  films grown on Si(111). *Thin Solid Films* 642:20–24. <https://doi.org/10.1016/j.tsf.2017.09.025>
- [32] Solovyov LA (2004) Full-profile refinement by derivative difference minimization. *J Appl Crystallogr* 37:743–749. <https://doi.org/10.1107/S0021889804015638>
- [33] Akselrud L, Cardoso Gil R, Wagner-Reetz M, Grin Y (2015) Disorder in the composite crystal structure of the manganese “disilicide”  $\text{MnSi}_{1.73}$  from powder X-ray diffraction data. *Acta Crystallogr Sect B Struct Sci Cryst Eng Mater* 71:707–712. <https://doi.org/10.1107/S2052520615019757>
- [34] Pretorius R, Theron CC, Vantomme A, Mayer JW (1999) Compound phase formation in thin film structures. *Crit Rev Solid State Mater Sci* 24:1–62. <https://doi.org/10.1080/10408439991329161>
- [35] Berche A, Tédenac J, Jund P (2014) First-principles determination of the enthalpy of formation of Mn–Si phases. *Solid State Commun* 188:49–52. <https://doi.org/10.1016/j.ssc.2014.02.021>
- [36] Aguf V, Pelleg J, Sinder M (2015) A note on the reaction between sputter co-deposited Mn and Si and formation of the  $\text{MnSi}$  phase. *AIP Adv* 5:67124. <https://doi.org/10.1063/1.4922449>
- [37] Allam A, Boulet P, Nunes CA, Record MC (2013) Investigation of new routes for the synthesis of  $\text{Mn}_4\text{Si}_7$ . *Metall Mater Trans A Phys Metall Mater Sci* 44:1645–1650. <https://doi.org/10.1007/s11661-013-1607-0>
- [38] Borisenko VE (2000) Semiconducting silicides. Springer Ser Mater Sci. <https://doi.org/10.1007/978-3-642-59649-0>
- [39] Zhang L, Ivey DG (1991) Low temperature reactions of thin layers of Mn with Si. *J Mater Res* 6:1518. <https://doi.org/10.1557/JMR.1991.1518>
- [40] Naito M, Nakanishi R, Machida N et al (2012) Growth of higher manganese silicides from amorphous manganese–silicon layers synthesized by ion implantation. *Nucl Instrum Methods Phys Res Sect B Beam Interact with Mater Atoms* 272:446–449. <https://doi.org/10.1016/j.nimb.2011.01.120>
- [41] Kajitani T, Yubuta K, Shishido T, Okada S (2010) Electron density distribution in  $\text{Mn}_4\text{Si}_7$ . *J Electron Mater* 39:1482–1487. <https://doi.org/10.1007/s11664-010-1210-8>
- [42] Klinger M (2017) More features, more tools, more CrysT-Box. *J Appl Crystallogr* 50:1226–1234. <https://doi.org/10.1107/S1600576717006793>
- [43] Lee J-H (2014) Significant enhancement in the thermoelectric performance of strained nanoporous Si. *Phys Chem Chem Phys* 16:2425–2429. <https://doi.org/10.1039/C3CP54632B>
- [44] Xu W, Liu Y, Chen B et al (2013) Nano-inclusions: a novel approach to tune the thermal conductivity of  $\text{In}_2\text{O}_3$ . *Phys Chem Chem Phys* 15:17595. <https://doi.org/10.1039/c3cp52942h>
- [45] Dai J, Spinu L, Wang K-Y et al (2000) Channel switching and magnetoresistance of a metal- $\text{SiO}_2$ -Si structure. *J Phys D Appl Phys* 33:L65–L67. <https://doi.org/10.1088/0022-3727/33/11/101>
- [46] Choi J, Nguyen VQ, Duong VT et al (2017) Formation of  $\text{Fe}_2\text{SiO}_4$  thin films on Si substrates and influence of substrate to its thermoelectric transport properties. *Phys B Condens Matter*. <https://doi.org/10.1016/j.physb.2017.05.025>
- [47] Teichert S, Kilper R, Erben J et al (1996) Preparation and properties of thin polycrystalline  $\text{MnSi}_{1.73}$  films. *Appl Surf Sci* 104–105:679–684. [https://doi.org/10.1016/S0169-4332\(96\)00223-1](https://doi.org/10.1016/S0169-4332(96)00223-1)
- [48] She X, Su X, Du H et al (2015) High thermoelectric performance of higher manganese silicides prepared by ultra-fast thermal explosion. *J Mater Chem C* 3:12116. <https://doi.org/10.1039/C5TC02837J>
- [49] Girard SN, Chen X, Meng F et al (2014) Thermoelectric properties of undoped high purity higher manganese silicides grown by chemical vapor transport. *Chem Mater* 26:5097–5104
- [50] Gorai P, Toberer ES, Stevanović V (2016) Thermoelectricity in transition metal compounds: the role of spin disorder. *Phys Chem Chem Phys* 18:31777–31786. <https://doi.org/10.1039/C6CP06943F>
- [51] Kim C-E, Soon A, Stampfl C (2016) Unraveling the origins of conduction band valley degeneracies in  $\text{Mg}_2\text{Si}_{1-x}\text{Sn}_x$  thermoelectrics. *Phys Chem Chem Phys* 18:939–946. <https://doi.org/10.1039/C5CP06163F>
- [52] Iioka M, Ishida D, Kojima S, Udono H (2013) Solution growth and optical characterization of  $\text{Mn}_{11}\text{Si}_{19}$ . *Phys status solidi* 10:1808–1811. <https://doi.org/10.1002/pssc.201300354>
- [53] Rebien M, Henrion W, Angermann H, Teichert S (2002) Interband optical properties of higher manganese silicide thin films. *Appl Phys Lett* 81:649. <https://doi.org/10.1063/1.1496135>
- [54] Migas DB, Borisenko VE (2013) Semiconducting silicides as potential candidates for light detectors: Ab initio predictions. *Phys Status Solidi Curr Top Solid State Phys* 10:1658–1660. <https://doi.org/10.1002/pssc.201300341>
- [55] Yablonskikh MV, Yarmoshenko YM, Gerasimov EG et al (2003) Local magnetic moments at X-ray spectra of 3d metals. *J Magn Magn Mater* 256:396–403. [https://doi.org/10.1016/S0304-8853\(02\)00974-5](https://doi.org/10.1016/S0304-8853(02)00974-5)
- [56] Kozina X, Karel J, Ouardi S et al (2014) Probing the electronic states of high-TMR off-stoichiometric  $\text{Co}_2\text{MnSi}$  thin films by hard X-ray photoelectron spectroscopy. *Phys Rev B* 89:125116. <https://doi.org/10.1103/PhysRevB.89.125116>

- [57] Yeh JJ, Lindau I (1985) Atomic subshell photoionization cross sections and asymmetry parameters:  $1 \leq Z \leq 103$ . Atomic Data Nucl Data Tables 32:1–155. [https://doi.org/10.1016/0092-640X\(85\)90016-6](https://doi.org/10.1016/0092-640X(85)90016-6)
- [58] Brar VW, Wickenburg S, Panlasigui M et al (2010) Observation of carrier-density-dependent many-body effects in graphene via tunneling spectroscopy. Phys Rev Lett 104:1–4. <https://doi.org/10.1103/PhysRevLett.104.036805>
- [59] Lischner J, Vigil-Fowler D, Louie SG (2013) Physical origin of satellites in photoemission of doped graphene: an Ab initio GW plus cumulant study. Phys Rev Lett 110:146801. <https://doi.org/10.1103/PhysRevLett.110.146801>
- [60] Lischner J, Pálsson GK, Vigil-Fowler D et al (2015) Satellite band structure in silicon caused by electron-plasmon coupling. Phys Rev B 91:205113. <https://doi.org/10.1103/PhysRevB.91.205113>
- [61] Kuzmenko A (2015) Guide to RefFit 1–127
- [62] Kuzmenko AB (2005) Kramers–Kronig constrained variational analysis of optical spectra. Rev Sci Instrum 76:83108. <https://doi.org/10.1063/1.1979470>